Variational numerical-modelling strategies for the simulation of driven free-surface waves

Yang Lu[1], Floriane Gidel[2], Junho Choi[3], Onno Bokhove[4], and Mark Kelmanson[1]

[1]School of Mathematics, University of Leeds, Leeds, UK
[2]SOPHiA Genetics, France
[3]Korea Advanced Institute of Science and Technology, Daejeon, South Korea
[4]School of Mathematics, Leeds Institute for Fluid Dynamics, University of Leeds, Leeds, LS2 9JT, UK

Correspondence: Onno Bokhove (o.bokhove@leeds.ac.uk)

Abstract. A new tool is developed for simulating three-dimensional (3D) water-wave motion using the first fully variational 3D discretisation in space and time of Luke's variational principle (VP), with additional focus on the formation and analysis of extreme waves generated within in-house experimental wavetanks. The resulting "numerical wavetank" is able to emulate laboratory sea states in which complex wave-wave and shoaling interactions occur. After first transforming the time-dependent free surface and oscillatory wavemaker into a static rectilinear domain with fixed boundaries using a σ-coordinate transformation, a fully-variational approach is used to derive a system of weak formulations that leads to a non-autonomous space-discrete Hamiltonian system to which robust (stable and mass-conserving) temporal integrators are applied. Specifically, time-discrete VPs with second-order Störmer-Verlet and modified-midpoint time-integration have been derived (and directly implemented through automation) in the finite-element environment *Firedrake* rather than their explicit weak forms, with spectrally-accurate higher-order finite elements. Verification and validation of the new tool are demonstrated via a novel convergence analysis and comparisons of its numerical results with a new analytical solution of three-dimensional two-soliton interaction as well as data post-processed from wavetank experiments.

1 Introduction

Extreme waves with high amplitudes, particularly rogue waves, may occur in heavy seas: the resulting loads or impact forces produced by such wave motions can lead to harsh marine environments that may put human lives, ships, and offshore structures at risk of serious damage and even destruction. Therefore, understanding and predicting high-amplitude waves and their impacts is of great significance in the field of maritime engineering, in which such waves are generated in physical wavetanks using wavemakers that simulate scaled-down model sea states. However, such experimental tests are usually high-cost and time-consuming to construct and calibrate, which invites consideration of more economical approaches based on mathematical and numerical modelling: this leads to the development of so-called *numerical* wavetanks (NWTs). Additionally, NWTs have attracted increasing consideration as a cost-effective testbed for the early-stage design, analysis and optimisation of wave-energy converters and ocean-renewable energy systems that may in the future play an important environmentally friendly means of dealing with the challenging problem of rising global-energy demands Ning et al. (2015); Windt et al. (2018).

Considerable effort has been invested in the development of numerical models based on potential-flow equations (PFEs) comprising the Laplace equation on the fluid volume under consideration, augmented by nonlinear kinematic and dynamic free-surface boundary conditions. By comparison with models based on the Navier-Stokes equations, the governing PFEs are significantly simplified due to their inherent assumptions of incompressible, inviscid and irrotational fluid flow; accordingly, fewer computational resources are required when carrying out PFE-based simulations. Moreover, comparisons with experimental investigations have shown that PFE-based numerical models are able to produce sufficiently accurate results that are relevant to practical problems. Hence, a balance between computational efficiency and accuracy can be achieved by the application of a nonlinear potential-flow model, for large temporal- and spatial-scale wave simulations Engsig-Karup et al. (2016).

Many prior PFE-based simulations of water waves and their interactions with solid boundaries have been conducted through (more conventional) numerical methods including, *inter alia*: boundary element methods (BEM) Grilli et al. (2001); Bai and Eatock Taylor (2006); Fochesato and Dias (2006); Fochesato et al. (2007); Ning et al. (2015); Grilli et al. (2020) in which only the domain boundary is discretised; field solvers, in which the entire domain is discretised, such as the finite difference method (FDM) Li and Fleming (1997); Bingham and Zhang (2007); Engsig-Karup et al. (2009); Wang et al. (2019), the finite volume method Lin et al. (2021), and the finite element method (FEM), the latter which is adopted in this work to be discussed separately. Apart from the classical FEM, high-order FEMs have also been developed for modelling nonlinear water-wave and wave-structure interactions, for example, the spectral-element method (SEM) Engsig-Karup et al. (2016); Engsig-Karup and Eskilsson (2019) and the spectral/*hp*-element method Karniadakis and Sherwin (2005); Xu et al. (2018).

In Wu and Eatock Taylor (1994, 1995) the FEM was used to solve nonlinear PFEs describing two-dimensional (2D) nonlinear free-surface wave dynamics driven by a piston wavemaker. The model in Wu and Eatock Taylor (1994, 1995) was extended to analyse sloshing waves in a three-dimensional (3D) rectangular tank undergoing translational motion Wu et al. (1998), and the FEM was also applied in Ma et al. (2001) to analyse non-linear 3D interactions between waves and fixed vertical cylinders.

A quasi arbitrary Lagrangian-Eulerian finite element method (QALE-FEM) was developed in Ma and Yan (2006) for simulating water waves based on fully nonlinear potential theory, thereby successfully overcoming the challenge of repeated re-meshing through a bespoke moving-mesh technique. The model in Ma and Yan (2006) was validated by simulating wavemaker-generate nonlinear waves, and their interactions with a geometrically complex seabed, and then used to simulate free nonlinear responses of 2D Yan and Ma (2007) and 3D Ma and Yan (2009) floating bodies to steep waves. A further development Yan and Ma (2010) was made to enable the QALE-FEM to model 3D overturning waves over complex seabeds efficiently. In Cai et al. (1998) a numerical method was developed for solving fully nonlinear water waves based on a domain-embedding approach that used a time-dependent mapping of the water volume onto a fixed solution domain.

In this study we present novel analyses and a computational tool for simulating 3D nonlinear water waves arising in two contexts: high-amplitude waves generated by in-house experimental wavetanks (at the Maritime Research Institute Netherlands), and; waves accruing from the interactions of 3D oblique solitons that can occur frequently in nature Ablowitz and Baldwin (2012); Kodama (2018). The analysis is based on a fully nonlinear potential-flow water-wave model, and the numerics are conducted through a consistent and novel space-time discretisation in 3D based on the governing variational principle and as

such implemented in the general finite-element environment *Firedrake* Ham et al. (2023); McRae et al. (2016); Bercea et al. (2016); Homolya and Ham (2016).

Accurate capturing of the formation and evolution of high-amplitude waves requires not only high-fidelity spatial-discretisation techniques but also robust temporal schemes in order to minimise dissipation caused by numerical simulations. Extra attention therefore needs to be paid when using the potential-flow model, wherein wave dynamics are considered in all three spatial dimensions. To fulfill our primary goal (of three) of pursuing improved modelling of nonlinear high-amplitude waves, this research draws on and builds upon a variational principle (VP) originally proposed by Luke Luke (1967), and successfully establishes a fully VP-based and as such novel approach in which consistent higher-order VP-based discretisations are employed in space and time in order to ensure the conservation of physical properties and to eliminate dissipation. In particular, one- to fourth-order continuous Galerkin (CG) *spectrally-accurate* Gauss-Lobatto-Legendre (GLL) polynomials, respectively CG1 to CG4, are used in the horizontal while in the vertical direction the same or even higher-order GLL-polynomials are deployed across a few elements or only one element. In addition, symplectic temporal-discretisation schemes —namely second-order modified-midpoint and Störmer-Verlet— are adopted in order to maintain stability and avoid energy drift in the simulations. The order of convergence, robustness and validation of the above-mentioned discretisation strategies are verified through a series of varied test cases ("TCs").

Wavemakers are widely used in the maritime industry to generate scheduled wave conditions in experimental wave basins: in our NWT, a piston wavemaker is considered so that wavemaker signals from real basin tests, e.g. time series of displacement, velocity and acceleration, can be applied directly as boundary conditions in the numerical simulations. Additionally, a non-uniform seabed is also taken into consideration. These two features, together with the potential-flow water-wave model, afford a physically faithful NWT (i.e., including the factual wavemaker motions), thereby fulfilling our second goal. However, they also raise the complexity of the NWT due to the presence of an *a priori* unknown free-surface elevation. That complexity is removed via the bespoke 3D σ-coordinate transformation acting on the free-surface in Li and Fleming (1997); Engsig-Karup et al. (2009); Cai et al. (1998). Here, it is extended to incorporate both the spatio-temporally varying wavemaker and seabed boundaries, with the physical domain transformed into a stationary computational domain within the VP. Hence, the mesh needs to be generated only once, at initialisation.

Our third and final goal is to verify and validate the NWT in five test cases (TCs) and make these openly accessible via online sharing (on GitHub) of source codes, with the aim of facilitating reproducibility and further development. When building the computational model using *Firedrake*, two approaches are adopted, the first of which follows the traditional path in which weak formulations are derived manually from the transformed VP and thereafter formulated explicitly in the code. By contrast, our second, and new, main approach is based on the *time-discretised* VP, for which the weak formulations are generated *automatically* and implemented implicitly using *Firedrake*'s inherent 'derivative' functionality; this approach both shortens the development time and reduces the risk of introduction of human error. The consistency between the two approaches, as confirmed by comparisons of several TCs, underpins the comparative accessibility of the latter. Moreover, by using an MPI call, the simulations can be performed in parallel with no additional changes or coding, courtesy of the in-built parallel computing features offered by *Firedrake*.

The flexibility of the present model lies in not only its capability of modelling various wavetank settings, but also its potential to be adapted to a wide range of problems. For example, the degree of the polynomials (i.e., the spatial order in horizontal and vertical directions) can be readily adjusted via amendment to the code. Moreover, by switching off the wavemaker and specifying a seabed, the NWT can be used to investigate wave-sloshing problems such as liquid motions in storage tanks Wu et al. (1998). If we take the further step of imposing periodic boundary conditions, the hitherto-finite wavetank becomes a semi-infinite pool wherein the interaction of solitons can be numerically investigated, as in TC5.

The outline of the remainder of this paper is as follows. The variational nonlinear potential-flow model is introduced in section 2, along with the 3D coordinate transformation leading to the transformed VP. The variational numerical model is developed in section 3 for implementation in *Firedrake*. The model is verified and validated via five TCs in section 4. It starts with standing-wave solutions of 2D linear PFEs (TC1), based on which (also new) spatial-temporal convergence analyses are performed both qualitatively (TC2a,b) and quantitatively (TC2c), followed by a 3D temporal convergence analysis with an oscillating wavemaker and a non-uniform seabed (TC3). The model is then validated against two test cases involving high-amplitude waves. The first uses experimental data provided by the Maritime Research Institute Netherlands (TC4 Bunnik (2010)). Seeding the PFEs with a newly devised analytical two-soliton-interaction solution of the Kadomtsev–Petviashvili equation (KPE) provides fourfold wave amplification (TC5), extending Choi et al. (2022). We close with a discussion.

2 Variational nonlinear potential-flow model

Water waves are often described by the Laplace equation for the velocity potential $\phi(x,y,z,t)$ as a function of horizontal coordinates x and y, vertical coordinate z and time t, augmented by two nonlinear boundary conditions (BCs): a kinematic BC, which expresses that the boundary moves with the fluid, and a dynamic BC, derived from the unsteady Bernouilli equation, which expresses the conservation of momentum. These equations describe the dynamics of the total water depth $h(x,y,t) = H(x,y)+\eta(x,y,t)$, where $H(x,y) = H_0 - b(x,y)$ is the depth at rest and $\eta(x,y,t)$ is the surface deviation from $H(x,y)$ with topography at $z = b(x,y)$, and of the velocity potential $\phi(x,y,z,t)$, which is defined such that the velocity field $\boldsymbol{u} = (u_x, u_y, u_z)$ is expressed as $\boldsymbol{u} = \nabla\phi$. In this study, the nonlinear, potential-flow equations

$$\nabla^2\phi = 0, \text{in } \Omega, \tag{1a}$$

$$\partial_t h + \nabla(h+b)\cdot\nabla\phi - \partial_z\phi = 0, \quad \text{at} \quad z = b(x,y)+h(x,y,t), \tag{1b}$$

$$\partial_t\phi + \frac{1}{2}|\nabla\phi|^2 + g(b+h-H_0) = 0, \quad \text{at} \quad z = b(x,y)+h(x,y,t), \tag{1c}$$

$$\partial_x\phi - \partial_y\phi\partial_y R = \partial_t R \quad \text{at} \quad x = R(y,t), \tag{1d}$$

where g is the gravitational constant, are obtained from Luke's variational principle Luke (1967) for an inviscid fluid:

$$0 = \delta\int_0^T\int_{\Omega_{x,y}}\int_{b(x,y)}^{b(x,y)+h(x,y,t)}\left[\partial_t\phi + \frac{1}{2}|\nabla\phi|^2 + g(z-H_0)\right]\mathrm{d}z\,\mathrm{d}x\,\mathrm{d}y\,\mathrm{d}t. \tag{2}$$

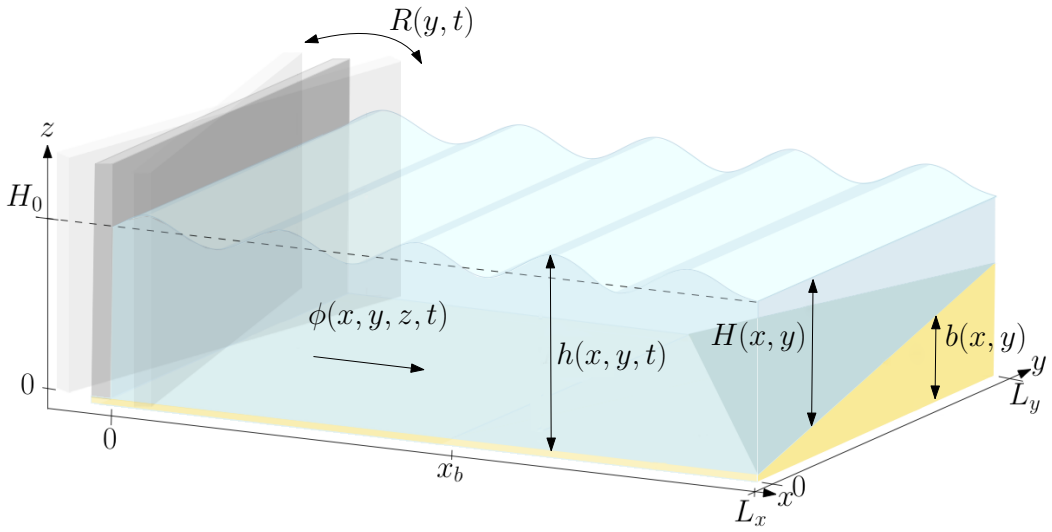

Figure 1. Schematic of the numerical wavetank. Waves are generated by a vertical piston wavemaker oscillating horizontally at $x = R(y,t)$ around $x = 0$. The depth at rest $H(x,y)$ varies in space due to the nonuniform seabed topography $b(x,y)$, here starting at $x = x_b$.

The horizontal domain $\Omega_{x,y} = \{R(y,t) \leq x \leq L_x; 0 \leq y \leq L_y\}$ is time-dependent due to the wavemaker boundary given by $x = R(y,t)$ (*cf.* Fig. 1). Similarly, the upper boundary of the domain, at $z = b(x,y) + h(x,y,t)$, moves around the rest depth $z = H_0$ with deviation $\eta(x,y,t)$ therefrom. We use the oceanographic convention with the free surface at rest residing at $z = H_0$. The numerical domain must therefore be discretized with a time-dependent mesh, with moving boundaries at $x = R(y,t)$ and $z = b(x,y) + h(x,y,t)$, noting that the water depth $h(x,y,t)$ is an unknown that itself needs to be solved as part of the solution. A σ-coordinate transformation akin to the one introduced by (Engsig-Karup et al., 2009) is used to solve the equations on a static domain, such that the transformed upper and moving wavemaker boundaries are fixed so that no mesh movement in the new vertical coordinate direction is required. Extending Engsig-Karup et al. (2009), we therefore introduce an additional coordinate transform in the x-direction to prevent the left-hand boundary from moving in the computational or transformed domain. The resulting computational domain, as represented in Fig. 2, is defined as

$$\hat{\Omega} = \{0 \leq \hat{x} \leq L_x; 0 \leq \hat{y} \leq L_y; 0 \leq \hat{z} \leq H_0\}, \tag{3}$$

where $H_0 = \max_{x \in \Omega_{x,y}} H(x,y)$. It is obtained from the initial domain

$$\Omega = \{R(y,t) \leq x \leq L_x; 0 \leq y \leq L_y; b(x,y) \leq z \leq h(x,y,t) + b(x,y)\}$$

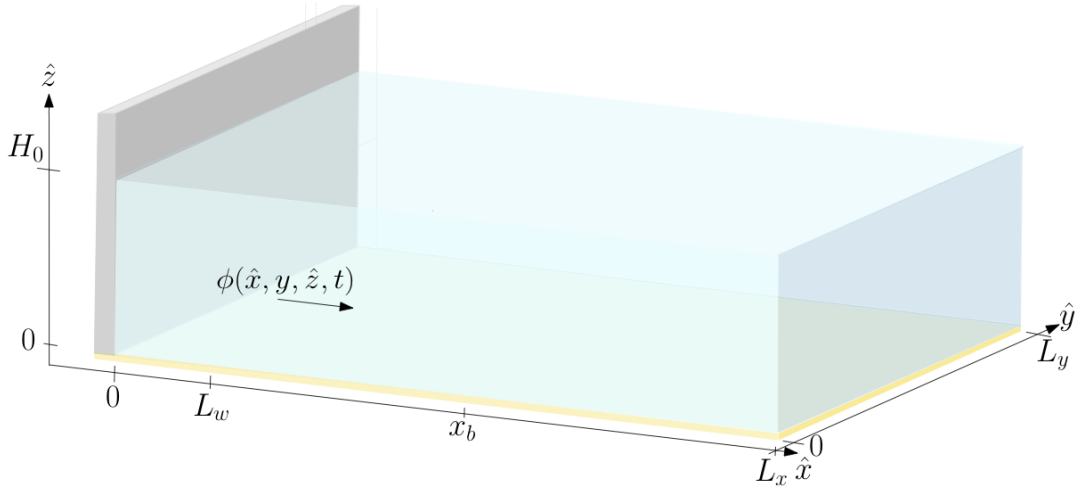

Figure 2. A depiction of the fixed, computational domain $\hat{\Omega}$ as defined by (3).

through the following transformations:

$$x \quad \rightarrow \quad \hat{x} = \frac{x - \tilde{R}(x,y,t)}{L_w - \tilde{R}(x,y,t)} L_w, \tag{4a}$$

$$y \quad \rightarrow \quad \hat{y} = y, \tag{4b}$$

$$z \quad \rightarrow \quad \hat{z} = (z - b(x,y)) \frac{H_0}{h(x,y,t)}, \tag{4c}$$

$$t \quad \rightarrow \quad \hat{t} = t, \tag{4d}$$

wherein $L_w = O(\lambda)$, with λ being a typical wavelength generated by the wavemaker and

$$\tilde{R}(x,y,t) = R(y,t)\,\Theta(L_w - x) = \begin{cases} R(y,t), & \text{if } x \leq L_w, \\ 0, & \text{if } x > L_w. \end{cases} \tag{5}$$

In Eq. (5), $\Theta(\cdot)$ denotes the Heaviside function such that the coordinate transform is effective in only the area $x \in [R(y,t), L_w]$, with $L_w = O(\lambda)$ as quantified above involving a typical wavelength λ: in this way, one can couple the water subdomain with the wavemaker without the need to transform in the x-direction for $L_w \leq x \leq L_x$. Note that the beginning of the seabed topography is set at $x = x_b \gg L_w$ so that $H(\hat{x}, \hat{y}) = H(x,y)$ since the horizontal domain is transformed only in the limited region near the wavemaker where the topography is constant, with $H(x,y) = H_0$. The transformation (4) ensures that the new vertical coordinate is everywhere $\hat{z} = [0, H_0]$, such that solutions are expanded on a fixed mesh.

Transforming variational principle (2) using (4), dropping hats and multiplying by a factor $H_0\,L_w$ leads to (*q.v.* Appendix A):

$$
\begin{aligned}
0 =& \delta \int_0^T \int_{\hat{\Omega}_{x,y}} \int_0^{H_0} \frac{1}{2}\frac{L_w^2}{W} h \Big(\phi_x - \frac{1}{h}\big(H_0 b_x + z h_x\big)\phi_z \Big)^2 \\
&+ \frac{1}{2} W h \Big(\frac{U}{W}\Big[\phi_x - \frac{1}{h}\big(H_0 b_x + z h_x\big)\phi_z\Big] + \phi_y - \frac{1}{h}\big(H_0 b_y + z h_y\big)\phi_z \Big)^2 \\
&+ \frac{1}{2} W \frac{H_0^2}{h} (\phi_z)^2 \\
&+ W h \Big(\phi_t - \frac{z}{h}\Big(\frac{X}{W}\tilde{R}_t h_x + h_t\Big)\phi_z + \frac{X}{W}\tilde{R}_t \phi_x + g(z\frac{h}{H_0} - H) \Big) \,\mathrm{d}z\,\mathrm{d}x\,\mathrm{d}y\,\mathrm{d}t,
\end{aligned}
\tag{6a}
$$

wherein subscripts denote partial differentiation and $\hat{\Omega}_{x,y}$ the fixed horizontal domain, i.e. $\hat{\Omega}_{x,y} = \{0 \le x \le L_x; 0 \le y \le L_y\}$, with

$$X(x) = x - L_w \tag{6b}$$

$$U(x,y,t) = X\,\tilde{R}_y(x,y,t), \tag{6c}$$

$$W(x,y,t) = L_w - \tilde{R}(x,y,t). \tag{6d}$$

The equivalent of the VP in Miles (Miles, 1977), in transformed coordinates is obtained, after using integrations by parts in x, z and t for the last four terms in (6a) and a sign reversal:

$$
\begin{aligned}
0 =& \delta \int_0^T \int_{\hat{\Omega}_{x,y}} \Big[H_0 \Big(\psi\big(W h_t + \underline{X\,\tilde{R}_t\,h_x}\big) - g W h (\frac{1}{2}h - H) \Big) \\
&- \int_0^{H_0} \frac{1}{2}\frac{L_w^2}{W} h \big(\phi_x - \frac{1}{h}\big(H_0 \underline{\underline{b_x}} + z h_x\big)\phi_z\big)^2 \\
&+ \frac{1}{2} W h \Big(\frac{U}{W}\Big[\phi_x - \frac{1}{h}\big(H_0 \underline{\underline{b_x}} + z h_x\big)\phi_z\Big] + \phi_y - \frac{1}{h}\big(H_0 \underline{\underline{b_y}} + z h_y\big)\phi_z \Big)^2 \\
&+ \frac{1}{2} W \frac{H_0^2}{h} (\phi_z)^2 \,\mathrm{d}z \Big] \mathrm{d}x\,\mathrm{d}y - \underline{\int_0^{L_y}\int_0^{H_0} \big(L_w\,\tilde{R}_t\,\phi\,h\big)|_{x=0} \mathrm{d}z\,\mathrm{d}y\,\mathrm{d}t},
\end{aligned}
\tag{7}
$$

in which we have introduced surface potential $\psi(x,y,t) \equiv \phi(x,y,z=H_0,t)$. Note that the term $-(x-L_w)\,R_t\,\delta(x-L_w)h\phi$, arising when integrating (6a) in x, is zero in the weak form, given that the contribution of $\delta(x-L_w)$ is zero due to the presence of the factor $(x-L_w)$. The transformed nonlinear potential-flow equations may be obtained from the variations of h and ϕ in (6a) or (7). Also, it should be noted that the double-underlined gradients of the topography b in the kinetic-energy expression in (7) can be ignored in a so-called *mild-slope approximation*, as employed by Gidel (2018). However, only simulations without this mild-slope approximation will be performed and analysed.

In more abstract form, (7) can be rewritten as follows

$$0 = \delta \int_0^T \left\{ \int_{\hat{\Omega}_{x,y}} H_0 W \psi h_t \,\mathrm{d}x\,\mathrm{d}y + \mathcal{H}[h,\psi,\phi,R] + \underline{\mathcal{R}[h,\psi,\phi,R]} \right\} \mathrm{d}t \tag{8}$$

with the underlined terms in (7) collected in $\mathcal{R}$, whilst $\mathcal{H}$ still depends on $R(t)$ (and thus explicitly on time t) but only through U and W, cf. (6c) and (6d).

3 Numerical model based on time-discrete variational principles

The next step is to formulate time-discrete versions of the variational principle (VP) (7) in the fixed coordinates used. Subsequently, these time-discrete VPs are implemented directly into the finite-element framework "Firedrake", using spectrally-accurate Gauss-Lobatto-Legendre (GLL) spatial polynomials on continuous-Galerkin function spaces. Automated yet partial variations (Alnaes, 2011; Alnaes et al., 2013) of these time-discrete VPs with finite-element GLL-expansions then directly and exactly yield the algebraically-complicated weak formulations. These variations are "partial" in that the bespoke Firedrake derivative-command takes care that the order of the highest derivatives present in the VP is preserved.

3.1 Time-discrete variational principles of second order in time and spectral accuracy in space

The time-discrete VPs for two second-order variational time-integrators are presented over one time-slab $t \in [t^n, t^n + \Delta t = t^{n+1}]$ with time node t^n, discrete $n = 0, 1, \ldots$ and fixed time-step Δt. The variational structure of (7) for wave fields in time is akin to the variational structure of a canonical classical-mechanical system, the latter with momentum and conjugate momentum as variables. Given that the time-discrete variational principle for the latter is readily derived over one time-slab for the modified-midpoint and Störmer-Verlet time-stepping schemes (Choi et al., 2024), one can immediately state the time-discrete VPs used. To deal with the explicit time-dependence in the VP (7), resulting it to be a non-autonomous system, time $t = t(\tau)$ is redefined as auxiliary variable, either as a "momentum" or "conjugate momentum" variable with a new pseudo-time τ. In either case, the (trivial) equation for the time evolution reads: $\mathrm{d}t/\mathrm{d}\tau = 1$ with initial condition $t(\tau = \tau_0) = t_0$ and $t_0 = \tau_0$ such that $t(\tau) = \tau$. This renders the non-autonomous system in time autonomous in auxiliary time τ. Subsequently, these geometric time-stepping schemes for autonomous variational or Hamiltonian systems can be applied.

The implementation into Firedrake requires the following partitioning of the velocity potential

$$\phi(x,y,z,t) = \psi(x,y,t)\hat{\phi}(z) + \varphi(x,y,z,t) \tag{9}$$

into a free-surface potential $\psi(x,y,t) = \phi(x,y,z = H_0,t)$ with vertical structure function $\hat{\phi}(z)$ obeying $\hat{\phi}(z = H_0) = 1$ at the (transformed) free surface $z = H_0$, and a homogeneous Dirichlet boundary condition on $\varphi(x,y,z = H_0,t) = 0$. In terms of these reformulated variables, the modified-midpoint (MMP) time-discrete VP for potential-flow dynamics over one time-slab

reads

$$
\begin{aligned}
0 =& \delta \Bigg\{ \int\limits_{\hat{\Omega}_{x,y}} \Bigg[H_0 \Big(\psi^{n+1/2} W^{n+1/2} \frac{h^{n+1} - h^n}{\Delta t} - h^{n+1/2} \frac{\psi^{n+1} W^{n+1} - \psi^n W^n}{\Delta t} \\
&+ \psi^{n+1/2} X \, \tilde{R}_t^{n+1/2} h_x^{n+1/2} - g W^{n+1/2} h^{n+1/2} \Big(\frac{1}{2} h^{n+1/2} - H \Big) \Big) \\
&- \int\limits_0^{H_0} \frac{1}{2} \frac{L_w^2}{W^{n+1/2}} h^{n+1/2} \Big(\hat{\phi} \psi_x^{n+1/2} + \varphi_x^{n+1/2} - \frac{1}{h^{n+1/2}} \big(H_0 \underline{\underline{b}}_x + z h_x^{n+1/2} \big) \Big(\psi^{n+1/2} \hat{\phi}_z + \varphi_z^{n+1/2} \Big) \Big)^2 \\
&+ \frac{1}{2} W^{n+1/2} h^{n+1/2} \Bigg(\frac{U^{n+1/2}}{W^{n+1/2}} \Big[\hat{\phi} \psi_x^{n+1/2} + \varphi_x^{n+1/2} - \frac{1}{h^{n+1/2}} \big(H_0 \underline{\underline{b}}_x + z h_x^{n+1/2} \big) \Big(\psi^{n+1/2} \hat{\phi}_z + \varphi_z^{n+1/2} \Big) \Big] \\
&\quad + \hat{\phi} \psi_y^{n+1/2} + \varphi_y^{n+1/2} - \frac{1}{h^{n+1/2}} \big(H_0 \underline{\underline{b}}_y + z h_y^{n+1/2} \big) \Big(\psi^{n+1/2} \hat{\phi}_z + \varphi_z^{n+1/2} \Big) \Bigg)^2 \\
&+ \frac{1}{2} W^{n+1/2} \frac{H_0^2}{h^{n+1/2}} \Big(\psi^{n+1/2} \hat{\phi}_z + \varphi_z^{n+1/2} \Big)^2 \mathrm{d}z \Bigg] \mathrm{d}x \, \mathrm{d}y \\
&- \int\limits_0^{L_y} \int\limits_0^{H_0} \Big(L_w \, \tilde{R}_t^{n+1/2} \Big(\psi^{n+1/2} \hat{\phi} + \varphi^{n+1/2} \Big) h^{n+1/2} \Big)_{x=0} \mathrm{d}z \, \mathrm{d}y \Bigg\},
\end{aligned}
\tag{10a}
$$

wherein variations are taken with respect to $\{h^{n+1/2}, \psi^{n+1/2}, \varphi^{n+1/2}\}$. Subsequently, we impose

$$
h^{n+1} = 2h^{n+1/2} - h^n \quad \text{and} \quad \psi^{n+1} = 2\psi^{n+1/2} - \psi^n. \tag{10b}
$$

The last two linear equations are used to eliminate $\{h^{n+1}, \psi^{n+1}\}$, whereafter the fully coupled system is solved for $\{h^{n+1/2}, \psi^{n+1/2}, \varphi^{n+1/}$ to enable the final update for $\{h^{n+1}, \psi^{n+1}\}$. Starting at $n = 0$, initial conditions for $\{h, \psi\}$ are used.

The Störmer-Verlet (SV) time-discrete VP for potential-flow dynamics over one time-slab reads (i.e., the time-discrete VP for (52) derived in Bokhove and Kalogirou (2016) is used here)

$$
\begin{aligned}
0 =& \delta\Bigg\{ \int_{\hat{\Omega}_{x,y}} \Bigg[H_0 \Bigg(\psi^{n+1/2} W^{n+1/2} \frac{h^{n+1}-h^n}{\Delta t} - \psi^{n+1} W^{n+1} \frac{h^{n+1}}{\Delta t} + \psi^n W^n \frac{h^n}{\Delta t} \\
&\quad + \psi^{n+1/2} X^{n+1/2} \tilde{R}_t^{n+1/2} \frac{1}{2}\Big(h_x^{n+1}+h_x^n\Big) - \frac{1}{2} g W^{n+1/2} \Big[h^{n+1}\Big(\frac{1}{2}h^{n+1}-H\Big) + h^n\Big(\frac{1}{2}h^n - H\Big)\Big]\Bigg) \\
&- \frac{1}{2}\int_0^{H_0} \frac{1}{2}\frac{L_w^2}{W^{n+1/2}} h^{n+1} \Big(\psi_x^{n+1/2}\hat{\phi} + \varphi_x^{n+1/2} - \frac{1}{h^{n+1}}\big(H_0 \underline{\underline{b_x}} + z h_x^{n+1}\big)\Big(\psi^{n+1/2}\hat{\phi}_z + \varphi_z^{n+1/2}\Big)\Big)^2 \\
&+ \frac{1}{2}\frac{L_w^2}{W^{n+1/2}} h^n \Big(\psi_x^{n+1/2}\hat{\phi} + \varphi_x^{n+1/2} - \frac{1}{h^{n}}\big(H_0 \underline{\underline{b_x}} + z h_x^{n}\big)\Big(\psi^{n+1/2}\hat{\phi} + \varphi_z^{n+1/2}\Big)\Big)^2 \\
&+ \frac{1}{2} W^{n+1/2} h^{n+1} \Bigg(\frac{U^{n+1/2}}{W^{n+1/2}} \Big[\psi_x^{n+1/2}\hat{\phi} + \varphi_x^{n+1/2} - \frac{1}{h^{n+1}}\big(H_0 \underline{\underline{b_x}} + z h_x^{n+1}\big)\Big(\psi^{n+1/2}\hat{\phi}_z + \varphi_z^{n+1/2}\Big)\Big] \\
&\quad + \psi_y^{n+1/2}\hat{\phi} + \varphi_y^{n+1/2} - \frac{1}{h^{n+1}}\big(H_0 \underline{\underline{b_y}} + z h_y^{n+1}\big)\Big(\psi^{n+1/2}\hat{\phi}_z + \varphi_z^{n+1/2}\Big)\Bigg)^2 \\
&+ \frac{1}{2} W^{n+1/2} h^{n} \Bigg(\frac{U^{n+1/2}}{W^{n+1/2}} \Big[\psi_x^{n+1/2}\hat{\phi} + \varphi_x^{n+1/2} - \frac{1}{h^{n}}\big(H_0 \underline{\underline{b_x}} + z h_x^{n}\big)\Big(\psi^{n+1/2}\hat{\phi}_z + \varphi_z\Big)\Big] \\
&\quad + \psi_y^{n+1/2}\hat{\phi} + \varphi_y^{n+1/2} - \frac{1}{h^{n}}\big(H_0 \underline{\underline{b_y}} + z h_y^{n}\big)\Big(\psi^{n+1/2}\hat{\phi}_z + \varphi_z^{n+1/2}\Big)\Bigg)^2 \\
&+ \frac{1}{2} W^{n+1/2} \frac{H_0^2}{h^{n+1}}\Big(\psi^{n+1/2}\hat{\phi}_z + \varphi_z^{n+1/2}\Big)^2 + \frac{1}{2} W^{n+1/2} \frac{H_0^2}{h^{n}}\Big(\psi^{n+1/2}\hat{\phi}_z + \varphi_z^{n+1/2}\Big)^2 \mathrm{d}z \Bigg] \mathrm{d}x\,\mathrm{d}y \\
&- \frac{1}{2}\int_0^{L_y}\int_0^{H_0} \Big(L_w \tilde{R}_t^{n+1/2}\Big(\psi^{n+1/2}\hat{\phi} + \varphi^{n+1/2}\Big)\Big(h^{n+1}+h^n\Big)\Big)_{x=0} \mathrm{d}z\,\mathrm{d}y \Bigg\},
\end{aligned}
\tag{11}
$$

in which variations are taken with respect to $\{h^n, \varphi^{n+1/2}\}$ to update $\{\psi^{n+1/2}, \varphi^{n+1/2}\}$ in unison, then $\psi^{n+1/2}$ to update h^{n+1}, and finally h^{n+1} to update to ψ^{n+1}. These time-discrete VPs (10a) and (11) are directly implemented into Firedrake with spectral GLL continuous-Galerkin finite-element expansions of the fields involved. The weak formulations are then derived in automated fashion, thus reducing time-to-development and human error.

The partitioning of the velocity field can be used in various ways. One can take $\hat{\phi}(z) = 1$ and use multiple elements in the vertical, with the same or different GLL-polynomial order in the horizontal and vertical. Or one can have only one element in the vertical and exclusively use the GLL higher-order polynomial $\hat{\phi}(z)$ with $\hat{\phi}(z = H_0) = 1$ of order p, as well as lower-order, different GLL-polynomials per element in the horizontal. The latter is akin to the variational discretisation in Gidel (2018), who exclusively used weak formulations stemming from a VP and standard Lagrange polynomials in one vertical element, which procedure suffers from Runge-effects for higher-order standard Lagrange polynomials. For intermediate and shallow-water waves, higher-order p-refinement over one element may be advantageous but that requires further investigation.

For the SV scheme the time-step restriction, based on analysis of a harmonic oscillator with frequency $\omega_{\max}$ (cf. Hairer et al. (2003)), is Gidel (2018)

$$\Delta t = CFL(2/\omega_{\max}), \tag{12}$$

with Courant number $CFL < 1$, whereafter we use the dispersion relation for linear water waves, $\omega_{\max} \approx \sqrt{gk\tanh(kH_0)}$, together with wavenumber $k = 2\pi/\Delta x$ in order to estimate the corresponding minimum mesh resolution Δx. The MMP-scheme is linearly unconditionally stable (it is then a Crank-Nicolson scheme) but the time-step used is essentially the same as the one for SV.

4 Verification and validation of the numerical model

Different aspects of the numerical model will be verified and validated via five test cases (TCs). In TC1, it is verified against exact standing-wave solutions of linear, potential-flow equations in the absence of a wavemaker and above flat-bottom topography. Spatial and temporal convergence analyses in 3D are then undertaken in the presence of an oscillating wavemaker and non-uniform seabed topography for TC2 and TC3. The model is validated against 2D freely available wave-tank measurements concerning wave groups propagating over a flat-bottom topography (TC4). A final 3D test case TC5 involves two-soliton interactions with maximum fourfold wave amplification.

4.1 TC1: Verification against standing-wave solution

To directly verify the accuracy, effectiveness and reliability of the computational model, the code is first tested against exact standing-wave solution of 2D *linear* potential-flow equations for the case with a resting wavemaker and flat bottom:

$$\nabla^2\phi = 0 \quad \text{on} \quad \Omega, \tag{13a}$$

$$\partial_t\eta = \partial_z\phi \quad \partial_t\phi = -g\eta \quad \text{at} \quad z = H_0. \tag{13b}$$

The exact standing-wave solutions of (13) for η and ϕ in a rectangular domain $(x,z) \in L_x \times H_0$ are given by

$$\eta(x,t) = \cos(kx)[A\cos(\omega t) + B\sin(\omega t)], \tag{14a}$$

$$\phi(x,z,t) = \cos(kx)(\mathrm{e}^{kz} + \mathrm{e}^{-kz})[-A\sin(\omega t) + B\cos(\omega t)]/\omega, \tag{14b}$$

where $k = 2\pi m/L_x$ is the wave number with m a positive integer, and the dispersion relationship is

$$\omega = \sqrt{gk\tanh(kH_0)}. \tag{14c}$$

Both the modified-midpoint and Störmer-Verlet time-stepping schemes are implemented in TC1, and the unknowns are initialized with (14a) and (14b). In the *Firedrake* environment, the partition (9) is implemented in the following way: one element with Lagrange polynomial of order n_z is adopted in the vertical direction, and $\hat{\phi}(z)$ is chosen to be a GLL polynomial

in the same order. The numerical computation is performed with $L_x = 2\pi$, $m = 2$, $A = B = 0.01$ (thus determining the initial conditions) and, given $H_0 = 1.137$ with $\cosh(kH_0) = g/2$, (14c) determines ω. The number of elements in the x-direction and the nodes in the vertical direction are set as $N_x = 126$ and $N_z = n_z + 1 = 7$, respectively. The time step is set as $\Delta t = \min\{\Delta x, \Delta z\}/\pi$. The simulation stops at $t = 3T_p$, with period $T_p = 2\pi/\omega$. For both schemes, the comparison between the nonlinear numerical solutions and (linearly) exact standing-wave solutions for $h(x = 0, t)$, $\phi(x = 0, z = 0, t)$ and $\phi(x = 0, z = H_0, t)$ over time are shown in the second and third row of Fig. 3, plotted as dashed and solid lines respectively. Numerical results agree well with exact solutions for both schemes.

We also monitor the energy evolution of the system over time, which is shown in the top row of Fig. 3 for the two schemes in blue solid lines, to verify the consistency of the temporal schemes. It can be seen that for both schemes the energy shows no drift and has bounded oscillations, while the amplitude for the case using the modified-midpoint scheme is much smaller than that obtained when using the Störmer-Verlet scheme. Logically, for this nearly linear test, since the former scheme has exact energy conservation in the linear limit. In addition, the energy evolution is also recorded when case TC1 is recomputed with a halved time resolution, for which the corresponding results are shown as cyan lines in Fig. 3. It can thus seen from the quadratic decreases in energy variations that both schemes have second-order temporal accuracy.

4.2 TC2: Convergence analyses

In this section, discussions build on the same problem considered in TC1, but the focus is shifted to examining the order of convergence for the present model. Specifically, convergence analyses are performed to investigate the effects of three factors, i.e., horizontal mesh resolution Δx, vertical structure n_z and time resolution Δt, on the numerical error, in which process the order of accuracy in space and time for the model emerges. The order of convergence will not only be studied qualitatively but also quantitatively. The former is backed by a reference solution whereas an approximated evaluation can be obtained by the latter approach.

4.2.1 TC2a: Spatial convergence analysis

Interpolation with first-order continuous Galerkin (Lagrange) polynomials (CG1) yields second-order spatial accuracy Smith (1978). To verify this spatial accuracy, we solve the nonlinear potential-flow equations with the modified-midpoint scheme in a 2D domain with initial conditions specified with (14a) and (14b).

Serving as the foundation, a computation on a rather fine spatial and temporal resolution is conducted, whose results are taken as the reference solution u_{ref}, based on which the errors of the subsequent simulations can be quantified. This resolution is set as $N_{x,f} = 3200$, $n_z = 64$ and $\Delta t_f = \Delta x_f/2\pi$ with $\Delta x_f = L_x/N_{x,f}$, where the subscript f denotes the *finest*. The error against u_{ref} will be measured by L^2- and L^∞-norms, and they are evaluated based on the discrete field data as follows:

$$\mathcal{E}_{L^2}(u^n) \equiv ||u^n - u^n_{\mathrm{ref}}||_2 = \sqrt{\sum_i \left(u^n_i - u^n_{\mathrm{ref},i}\right)^2}, \quad \text{and}$$
$$\mathcal{E}_{L^\infty}(u^n) \equiv ||u^n - u^n_{\mathrm{ref}}||_\infty = \max_i |u^n_i - u^n_{\mathrm{ref},i}|, \tag{15}$$

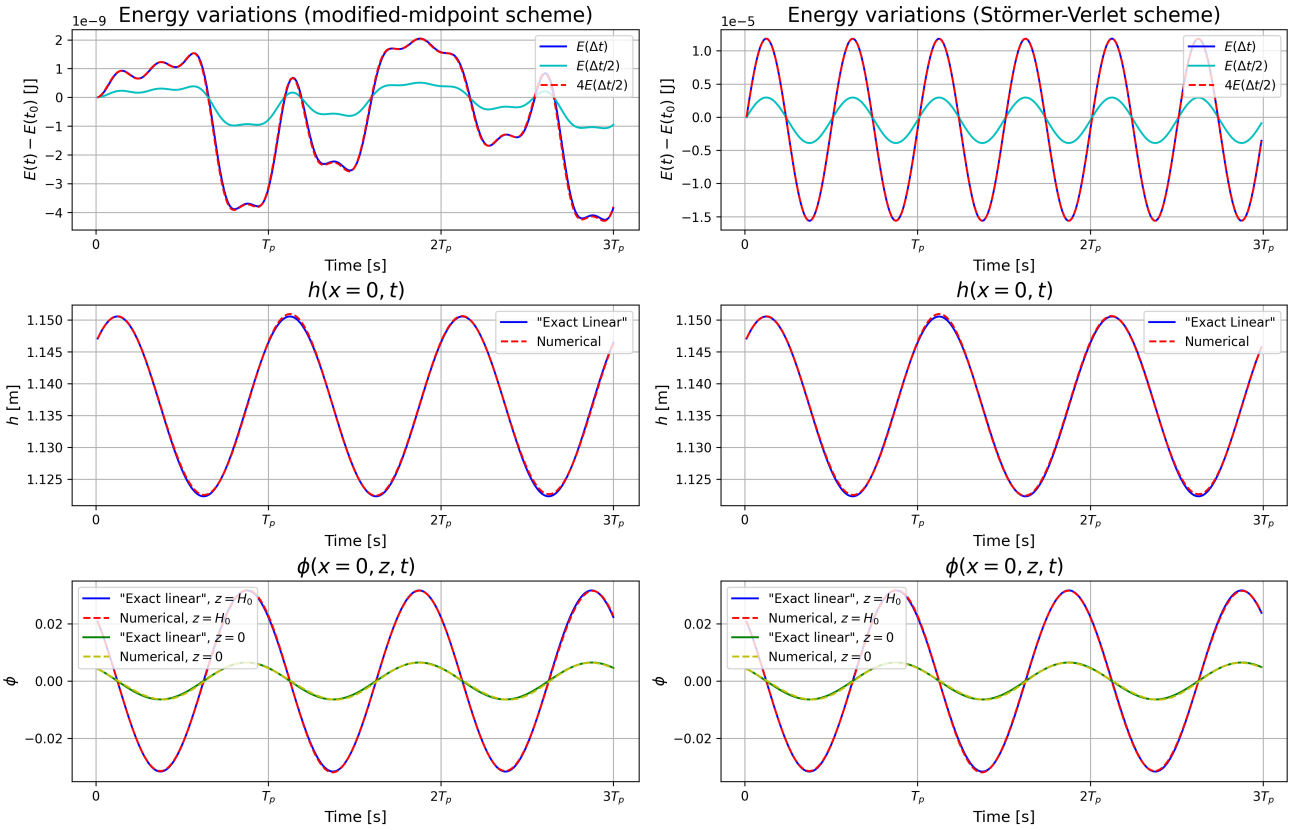

(a) Modified-midpoint scheme (b) Störmer-Verlet scheme

Figure 3. TC1: Energy variations (top row) and comparison between the numerical solutions and exact standing-wave solutions of linear potential-flow equations (middle and bottom rows) using (a) modified-midpoint and (b) Störmer-Verlet time-stepping schemes.

where u^n represents the numerical solutions at time t^n and i designates the discrete evaluation points. Solutions of water depth $h(x_i, t^n)$ and free-surface velocity potential $\psi(x_i, t^n)$ are evaluated at the vertices of this finest horizontal mesh in subsequent simulations.

A series of computations with five different horizontal resolutions are conducted to verify the order of convergence in space (TC2a). Starting with $N_x = 50$, the mesh is refined by doubling the number of elements till $N_x = 800$, whereas $n_z = 32$ and $\Delta t = 2\Delta t_f$ remain unchanged. L^2- and L^∞-errors $\mathcal{E}_{L^2}$ and $\mathcal{E}_{L^\infty}$, computed for solutions h_i and ψ_i at $t = 3T_p \approx 4.3$s, are respectively shown in Figs. 4(a,b). By comparison against the red reference line with slope 2, it can be seen that the error decreases quadratically upon mesh refinement. Hence, CG1 yields second-order accuracy in space.

A preliminary investigation is also carried out on the Lagrangian-interpolation error of the vertical discretisation. n_z is varied between 2 and 32 while $N_x = 800$ and temporal resolution $\Delta t = 2\Delta t_f$ are fixed. Errors calculated from h_i and ψ_i at $t = 3T_p$ are shown in Figs. 4(c,d) in semi-log scale. It suggests that the error decreases exponentially as the order of the polynomial n_z increases, but then reaches a plateau when $n_z \geq 6$, where the overall error is dominated by other factors. Given that the two

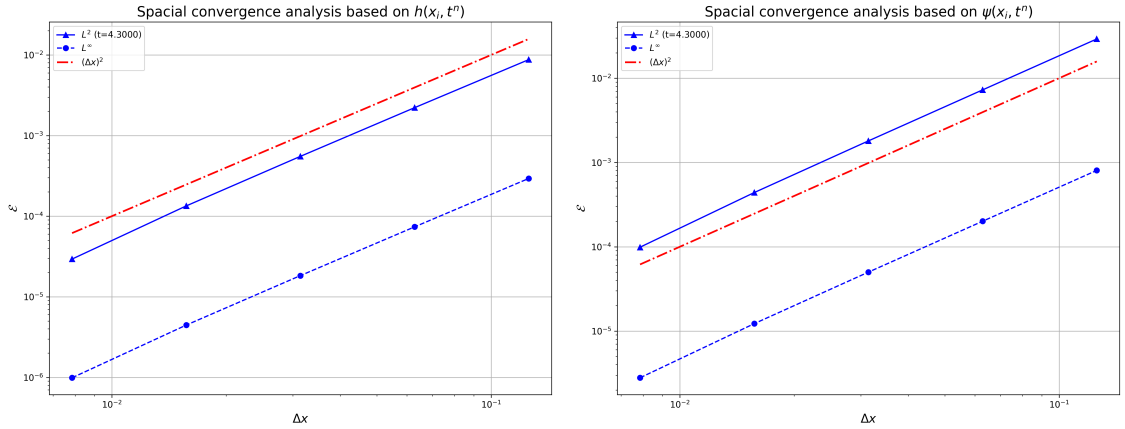

(a) TC2a: Effect of Δx on error of h. (b) TC2a: Effect of Δx on error of ψ.

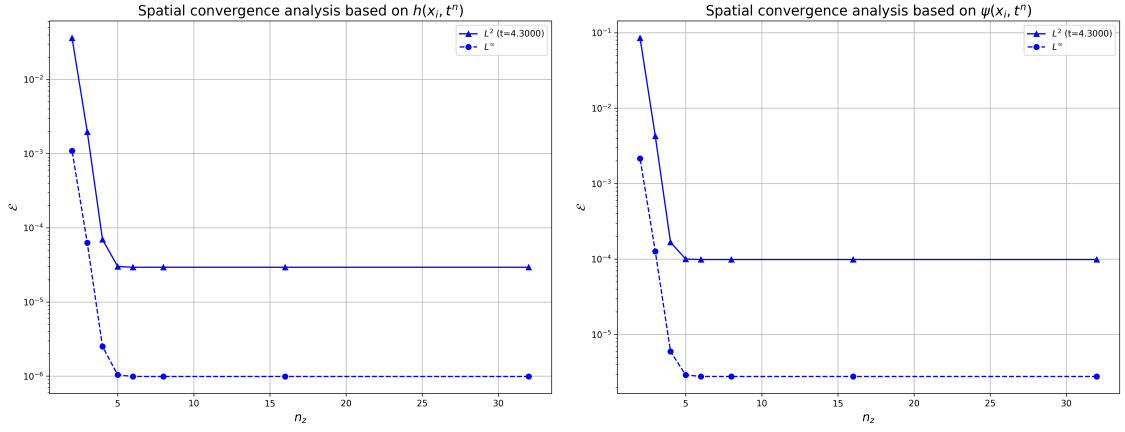

(c) Effect of n_z on error of h. (d) Effect of n_z on error of ψ.

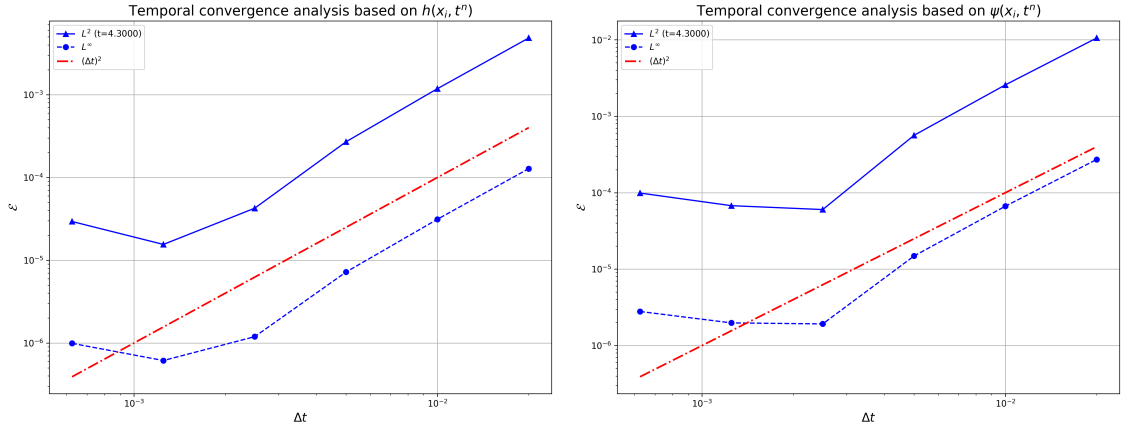

(e) TC2b: Effect of Δt on error of h. (f) TC2b: Effect of Δt on error of ψ.

Figure 4. TC2a,b: Investigations on the effects of Δx (top row (a,b)), n_z (middle row (c,d)) and Δt (bottom row (e,f)) on the error measured by L^2- and L^∞-norms. Figures in the left and the right column are based on the free-surface solutions $h(x_i, t = 4.3)$ and $\psi(x_i, t = 4.3)$, respectively.

rightmost points at the edge of the plateau in Fig. 4(c) (Fig. 4(d)) and the two leftmost ones in Fig. 4(a) (Fig. 4(b)) are obtained from the finest mesh in TC2a and correspond to the same computation, the occurrence of the plateau is attributed to the (finite) horizontal resolution used here.

4.2.2 TC2b: Temporal convergence analysis

Following TC2a, the order of convergence in time can be similarly verified. Six refining-by-halving temporal resolutions are selected with Δt decreasing from $64\Delta t_f$ to $2\Delta t_f$, while the spatial resolution remains unchanged, with $N_x = 800$ and $n_z = 32$. Results at $t = 3T_p$ are shown in Figs. 4(e.f). At the first stage when $\Delta t \geq 16\Delta t_f$, the error decreases in parallel with the red reference line of slope 2, indicating that the time-stepping scheme is second-order. As the time step becomes smaller, the error diverges from the quadratic relationship and a further decline is suppressed. This may partly be attributed to the chosen spatial resolution. More importantly, it raises the concern that the reference solution is also based on a finite (although fine) resolution and consequently, there exists an inherent error accompanying u_{ref}. This drawback will be overcome with the approach presented in TC2c, where u_{ref} is not required.

4.2.3 TC2c: Advanced and novel convergence analysis

A spatio-temporal convergence analysis can be conducted by assuming that the computed u at a chosen point (x, z, t) in space and time has a truncation error, relative to the exact value u_0, that is a linear combination of errors in the individual variables, namely

$$u - u_0 = A(\Delta x)^p + B(\Delta t)^q + C_{n_z}, \tag{16}$$

in which A, B, p and q are constants and the Lagrangian-interpolation error is of the usual form

$$C_{n_z} = \frac{u_0^{(n_z+1)}(\zeta)}{(n_z+1)!} \prod_{i=0}^{n_z} (z - z_i), \tag{17}$$

in which the z_i are the interpolation nodes and $\zeta \in [z_0, z_{n_z}]$. Thus, in contrast to the locally constant coefficients comprising the errors in x and t, the leading error in z is a polynomial that depends upon the global distribution of nodes, which precludes explicit estimation of C_{n_z} in (16). However, progress can be made as follows.

For each point (x, z, t), we compute thirteen values of u using different resolutions Δx in the horizontal direction x, Lagrange-node count n_z in the vertical direction z, and time step Δt. Using the subscripts c, m and f to denote coarse,

medium and fine resolutions respectively in both x and t, the thirteen required numerical values are

$$\begin{aligned} &u_{crc} = u_{crc}(\Delta x = h, n_z = r, \Delta t = k) \qquad u_{mrc} = u_{mrc}(\Delta x = h/2, n_z = r, \Delta t = k) \\ &u_{frc} = u_{frc}(\Delta x = h/4, n_z = r, \Delta t = k) \quad u_{crm} = u_{crm}(\Delta x = h, n_z = r, \Delta t = k/2) \\ &u_{crf} = u_{crf}(\Delta x = h, n_z = r, \Delta t = k/4); \end{aligned} \tag{18a}$$

$$\begin{aligned} &u_{csc} = u_{csc}(\Delta x = h, n_z = s, \Delta t = k) \qquad u_{msc} = u_{msc}(\Delta x = h/2, n_z = s, \Delta t = k) \\ &u_{fsc} = u_{fsc}(\Delta x = h/4, n_z = s, \Delta t = k) \quad u_{csm} = u_{csm}(\Delta x = h, n_z = s, \Delta t = k/2) \\ &u_{csf} = u_{csf}(\Delta x = h, n_z = s, \Delta t = k/4); \end{aligned} \tag{18b}$$

$$\begin{aligned} &u_{cvc} = u_{cvc}(\Delta x = h, n_z = v, \Delta t = k) \qquad u_{mvc} = u_{mvc}(\Delta x = h/2, n_z = v, \Delta t = k) \\ &u_{cvm} = u_{cvm}(\Delta x = h, n_z = v, \Delta t = k/2), \end{aligned} \tag{18c}$$

wherein the three values of n_z in the above computations satisfies $v > s > r$. With the first five computed with $n_z = r$ in (18a), we calculate the two quantities

$$R_p = \frac{u_{crc} - u_{mrc}}{u_{mrc} - u_{frc}} \quad \text{and} \quad R_q = \frac{u_{crc} - u_{crm}}{u_{crm} - u_{crf}}, \tag{19}$$

using which yields

$$u_0 = \frac{R_p u_{mrc}}{R_p - 1} + \frac{R_q u_{crm}}{R_q - 1} - \frac{(R_p R_q - 1) u_{crc}}{(R_p - 1)(R_q - 1)} - C_r,\ \rho_x = \frac{\ln R_p}{\ln 2},\ \rho_t = \frac{\ln R_q}{\ln 2}, \tag{20}$$

which respectively correspond to the extrapolated value u_0 of u (i.e. as $\Delta x, \Delta t \to 0$ and $n_z \to \infty$), an estimation of the order of convergence in the x direction, and an estimation of the temporal order of convergence.

Although ρ_x in (20) holds for one point in space and time, the spatial order of convergence can still be evaluated based on the field data by replacing the differences in R_p's expression with suitable norms, which is eventually equivalent to the formula derived for the regularly refined-by-halving meshes from Atiken extrapolation Salwa et al. (2017a):

$$s = \log_2 \frac{\|u_m - u_c\|}{\|u_f - u_m\|}, \tag{21}$$

where only one subscript highlighting the horizontal resolution is kept for u; and $\|\cdot\|$ represents either the L^2 or L^∞-norm, as defined in (15).

It is then applied to the five computations in TC2a to verify the order of convergence in space, without consulting the reference solution this time. The results are summarized in Table 1. For any group, the error norm between u_f and u_m is approximately a quarter of that between u_m and u_c at any time over the whole time-period $t \in [0, 3T_p]$, resulting in an averaged $\bar{s} \approx 2$.

Recalling definition ρ_t in (20), the temporal order of convergence can also be evaluated by applying (21) onto three computations with refined-by-halving time steps, i.e., the triple $\{u_c, u_m, u_f\}$ in (21) now stands for solutions from coarse, medium and fine temporal resolutions, respectively. Based on computations in TC2b, the results for the temporal order of convergence are summarized in Table 2. It is verified again that the modified-midpoint scheme has second-order accuracy in time.

Data source	Groups of solutions $\{u_f, u_m, u_c\}$		
	$N_x \in \{800, 400, 200\}$	$N_x \in \{400, 200, 100\}$	$N_x \in \{200, 100, 50\}$
$h(x_i, t^n)$	1.9878; 1.9996	1.9965; 1.9984	1.9977; 1.9943
$\psi(x_i, t^n)$	1.9883; 1.9995	1.9965; 1.9979	1.9970; 1.9939

Table 1. TC2a revisited: Spatial order of convergence $\bar{s}_2$ and $\bar{s}_\infty$ averaged between $t = 0$ and $t = 3T_f$, calculated based on L^2-norm (before the semicolon) and L^∞-norm, respectively, using the five groups of solutions with regularly-halved horizontal mesh resolutions Δx in TC2a.

Data source	Groups of solutions $\{u_f, u_m, u_c\}$			
	$\Delta t \in \{2, 4, 8\}\Delta t_f$	$\Delta t \in \{4, 8, 16\}\Delta t_f$	$\Delta t \in \{8, 16, 32\}\Delta t_f$	$\Delta t \in \{16, 32, 64\}\Delta t_f$
$h(x_i, t^n)$	2.0000; 2.0000	2.0000; 1.9999	1.9998; 1.9997	1.9990; 1.9986
$\psi(x_i, t^n)$	2.0000; 2.0000	1.9999; 1.9999	1.9997; 1.9998	1.9986; 1.9988

Table 2. TC2b revisited: Temporal order of convergence $\bar{s}_2$ and $\bar{s}_\infty$ averaged between $t = 0$ and $t = 3T_p$, calculated based on L^2-norm (before the semicolon) and L^∞-norm, respectively, using the six groups of solutions with regularly-halved time steps Δt in TC2b.

In (20), it remains to estimate C_r. Because A and B in (16) are constants dependent upon the local value of x and t, they do not change with n_z for fixed x, t. Equivalently, neither do R_p and R_q. Thus, by the first equation in (20) and the three values in (18b) computed with $n_z = s$, there follows

$$u_0 = \frac{R_p u_{msc}}{R_p - 1} + \frac{R_q u_{csm}}{R_q - 1} - \frac{(R_p R_q - 1) u_{csc}}{(R_p - 1)(R_q - 1)} - C_s. \tag{22}$$

Subtracting the two expressions for u_0 then yields

$$C_r - C_s = \frac{R_p (u_{mrc} - u_{msc})}{R_p - 1} + \frac{R_q (u_{crm} - u_{csm})}{R_q - 1} - \frac{(R_p R_q - 1)(u_{crc} - u_{csc})}{(R_p - 1)(R_q - 1)}. \tag{23}$$

Based upon the (physically reasonable) assumption that variations in u are smoothly differentiable with respect to z to order $s+1$, the inverse-factorial decay of the truncation error (17) means that $|C_s| \ll |C_r|$ when $s > r$, and we thus approximate the left-hand side of (23) by C_r alone. Inserting this approximation of C_r in (23) into the expression for u_0 in (20) finally yields

$$u_0 \approx \frac{R_p u_{msc}}{R_p - 1} + \frac{R_q u_{csm}}{R_q - 1} - \frac{(R_p R_q - 1) u_{csc}}{(R_p - 1)(R_q - 1)}, \tag{24}$$

which reflects the negligibility of C_s in (22) and gives the value to which computations of u should converge. Specifically, the preliminary test on the effect of n_z (cf. Figs. 4(c,d)) offers *a posteriori* confirmation of the argument used to neglect C_s. The argument can be further verified by a slight extension of the above analysis.

In addition to the eight computations used above, five more are required, namely u_{fsc} and u_{csf} in (18b), along with u_{cvc}, u_{mvc} and u_{cvm} in (18c). For illustrative purposes, here the coarsest resolution, from which u_{crc} is computed, is selected as $N_x = 50$, $\Delta t = 64\Delta t_f$ and $r = 4$. The other two finer n_z are chosen as $s = 6$ and $v = 8$. Firstly using (23), $C_r - C_s$ can be

point-wisely evaluated at the free surface for h_i and ψ_i, with i denoting the vertices of the coarsest horizontal mesh. Following (23), $C_r - C_v$ can be evaluated straightforwardly by replacing the three computations using $n_z = s$ with the three in (18c), which reads

$$C_r - C_v = \frac{R_p(u_{mrc} - u_{mvc})}{R_p - 1} + \frac{R_q(u_{crm} - u_{cvm})}{R_q - 1} - \frac{(R_pR_q - 1)(u_{crc} - u_{cvc})}{(R_p - 1)(R_q - 1)}. \tag{25}$$

Given (23) and (25), $C_s - C_v$ can then be calculated indirectly through $(C_r - C_v) - (C_r - C_s)$. Alternatively, it can also be evaluated directly by going through the same procedure that finds $C_r - C_s$, except that the newly-required eight computations are those in (18b) and (18c).

The associated results are collected in Fig. 5, where the point-wise evaluations based on h_i and ψ_i are shown in the top row and bottom row respectively. For both solutions, the overall difference between C_s and C_v is approximately 10^3 times smaller than that between C_r and C_s (or C_v), which validates that C_s is negligible compared with C_r in this case. Furthermore, as illustrated in Figs. 5(b,d) the direct and indirect evaluations of $C_s - C_v$ agree well with each other, which verifies the consistency of the advanced analysis.

The consistency[1] can also be verified by finding an explicit form for C_{n_z}. The exponential relationship shown in Figs. 4(c,d) associated with orthogonal-polynomial interpolation, namely

$$C_{n_z} = Dc^{n_z}, \tag{26}$$

where D and c are constants for a given point and $c < 1$. Let $\{u_r, u_s, u_v\}$ represent a group of computations with $n_z = r < s < v$, but the same Δx and Δt. Using (16) and (26), we have

$$u_r - u_s = D(c^r - c^s) = Dc^r(1 - c^{s-r}) \text{ and } u_s - u_v = D(c^s - c^v) = Dc^s(1 - c^{v-s}). \tag{27}$$

It is therefore feasible to evaluate the constant c point-wisely based on the triple when $s - r = v - s$ through

$$c = \left(\frac{u_s - u_v}{u_r - u_s}\right)^{1/(s-r)}. \tag{28}$$

The evaluations from $\{u_{crc}, u_{csc}, u_{cvc}\}$, $\{u_{crm}, u_{csm}, u_{cvm}\}$ and $\{u_{mrc}, u_{msc}, u_{mvc}\}$, based on the solutions h_i (left) and ψ_i (right), are shown in Fig. 6, yielding that $c < 1$. To ensure the validity of (28), absolute values are taken for $u_s - u_v$ and $u_r - u_s$. Additionally, the three curves, which correspond to three groups of solutions with different resolutions, almost agree with each other at any point on the free surface, which again verifies the consistency of our advanced analysis, especially the exponential decay of the error caused by n_z.

4.3 TC3: Energy conservation and temporal convergence

The symplectic temporal schemes are, by construction, intended to yield stability and bounded energy oscillations and to preclude numerical dissipative drifts of energy. These energy fluctuations are now checked via computations using two time

[1]We kindly acknowledge Evy Kersalé's assistance herein.

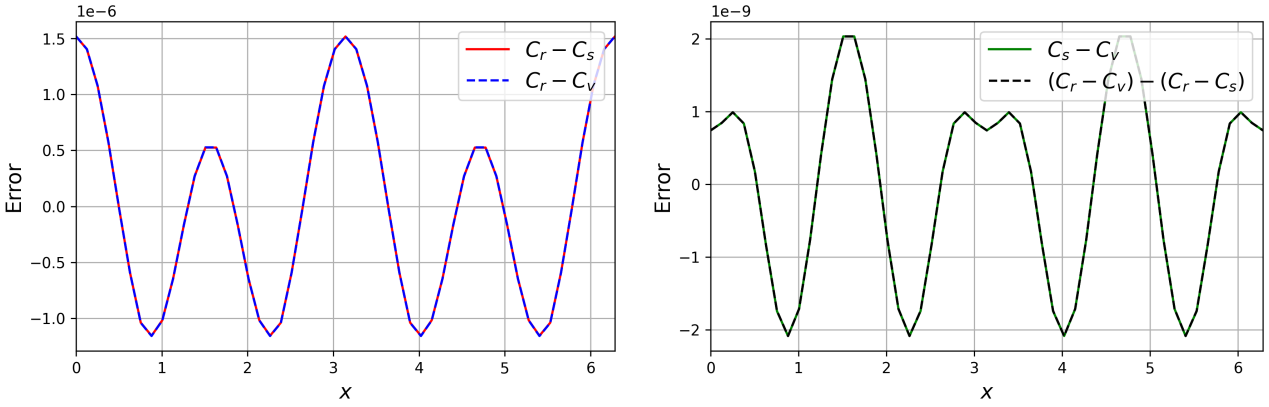

(a) Direct evaluation of $C_r - C_s$ and $C_r - C_v$ for h_i. (b) Indirect (dashed line) and direct (solid line) evaluations of $C_s - C_v$ for h_i.

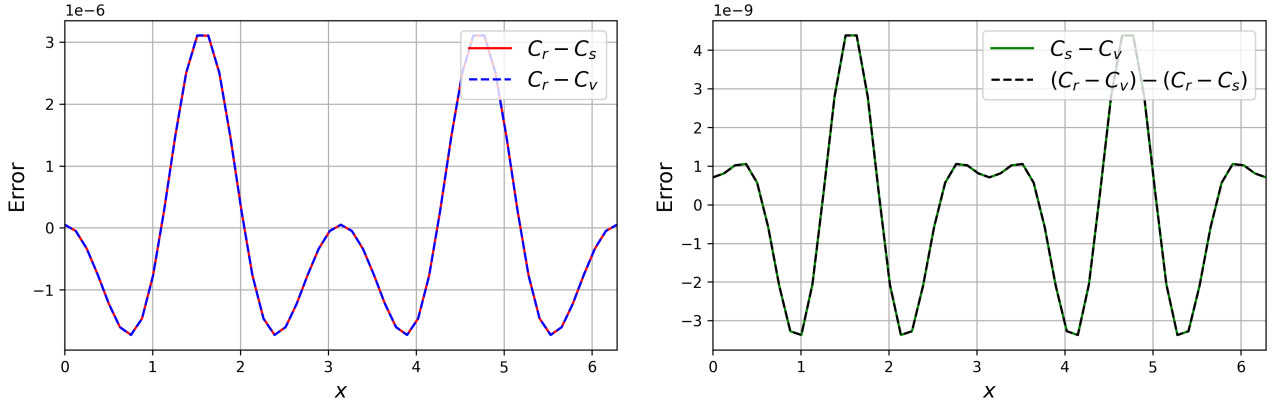

(c)

Direct evaluation of $C_r - C_s$ and $C_r - C_v$ for ψ_i. (d) Indirect (dashed line) and direct (solid line) evaluations of $C_s - C_v$ for ψ_i.

Figure 5. TC2c: Direct and indirect point-wise evaluations on the Lagrangian-interpolation error C_{n_z} based on the solutions $h(x_i, t = 3T_p)$ (top row (a,b)) and $\psi(x_i, t = 3T_p)$ (bottom row (c,d)), with $n_z \in \{r = 4, s = 6, v = 8\}$. The numerical solutions are collected at the vertices of the coarsest horizontal mesh.

resolutions, $\Delta t_1 = 0.001$s and $\Delta t_2 = 0.002$s, for the MMP-VP and SV schemes, denoted as MMP1 and MMP2, SV1 and SV2, respectively. Simulations are conducted in the time-period $t \in [0, 17]$s, and the wavemaker stops at $t = 5T_w = 5.670$s, where $T_w = 2\pi/\omega$ is the wavemaker period. Parameters used in TC3 are summarized in Table 3.

Energy evolutions obtained using (a) modified-midpoint and (b) Störmer-Verlet schemes for the two time resolutions are shown in Fig. 7. Initially at $t = 0$ the wavemaker is off and the water is at rest. Hence, there is no kinetic energy in the system; for the purposes of analysing only evolutionary changes, the potential energy has been offset to yield a zero datum. When the wavemaker starts moving, energy is input into the system and thus it increases until $t = t_{\text{stop}} = 5.670$s, when the wavemaker is turned off. This net gain of energy occurs because the wavemaker leads to energy transferring into the system, cf. definitions

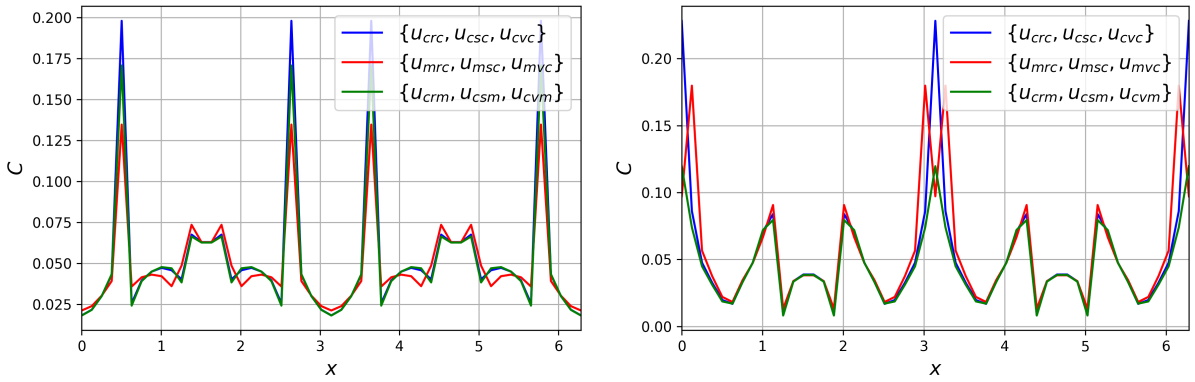

Figure 6. TC2c: point-wise evaluation of the constant c from three groups of $\{u_r, u_s, u_v\}$ satisfying $s - r = v - s$, with the left and right graph obtaining from the solutions $h(x_i, t = 3T_p)$ and $\psi(x_i, t = 3T_p)$ respectively.

Domain			Beach	
L_x [m]	L_y [m]	H_0 [m]	x_b [m]	s_b
6.5	1.0	1.0	4.0	0.2
Wavemaker				
λ [m]	ω [rad/s]	T_w [s]	γ [m]	L_w [m]
2.0	5.54	1.13	0.03	1.0
Resolutions				
Δx [m]	Δy [m]	n_z	Δt_1 [s]	Δt_2 [s]
0.05	0.05	8	0.001	0.002

Table 3. Parameters used in TC3. Dimensions are given in square brackets. Each simulation runs from $t = 0$s to $t = t_{\text{end}} = 17$s and the wavemaker is turned off at $t = t_{\text{stop}} = 5.670$s.

arising from (8) with (7), since

$$\frac{\mathrm{d}(\mathcal{H} + \mathcal{R})}{\mathrm{d}t} \neq 0. \tag{29}$$

Due to the wavemaker, the Hamiltonian depends explicitly on time. As a consequence the energy is not conserved, except when the wavemaker is turned off, since then $\mathcal{R} = 0$ with $R(t) = 0$ such that also $\mathrm{d}\mathcal{H}/\mathrm{d}t = 0$. This is illustrated with Fig. 7, where no energy drift is observed after switching off the wavemaker (for $t > t_{\text{stop}}$).

In Fig. 8, we verify the consistency of the temporal schemes by focussing on the energy variations after the wavemaker is switched off (*i.e.*, for $5.670\text{s} \leq t \leq 17\text{s}$). The Hamiltonian dynamics of our temporal schemes result in bounded and small-

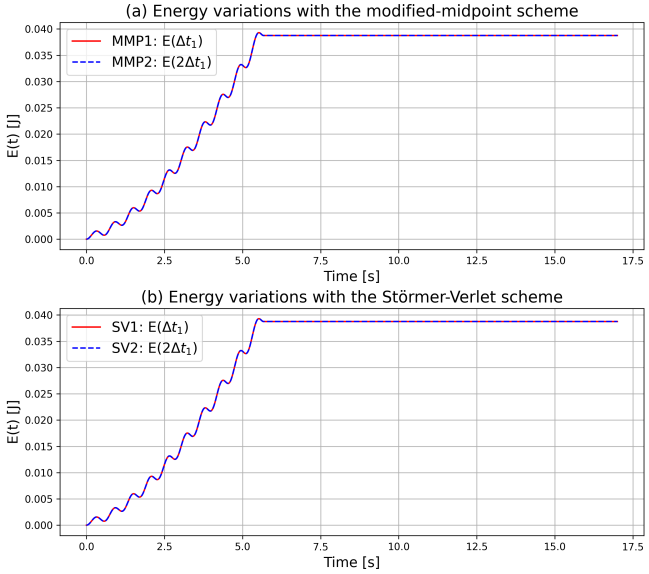

Figure 7. TC3: Energy evolutions of the four simulations using the (a) modified-midpoint and (b) Störmer-Verlet schemes. The wavemaker generates the waves from $t = 0$ to $t = t_{\text{stop}} = 5.670\text{s}$ and is then turned off. MMP1 and SV1 are computed with $\Delta t_1 = 0.001\text{s}$ (continuous red line), whereas in MMP2 and SV2 time resolution is set as $\Delta t_2 = 2\Delta t_1 = 0.002\text{s}$ (dashed blue line).

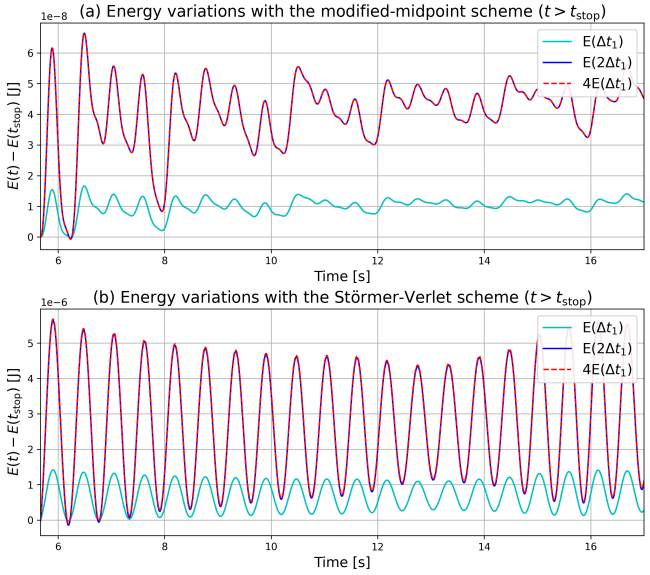

Figure 8. TC3: Energy variations with (a) modified-midpoint and (b) Störmer-Verlet schemes in the absence of wavemaker motion, i.e. $t > t_{\text{stop}}$. Continuous cyan lines show variations in cases MMP1 (a) and SV1 (b). Continuous blue lines show variations in cases MMP2 (a) and SV2 (b). The dashed red lines are four times the variations of MMP1 (a) and SV1 (b), respectively.

amplitude energy oscillations. For both schemes, the amplitude of these oscillations diminishes for smaller time steps, whereas for the same time resolution the energy variations obtained with MMP are about 100 times smaller than those obtained with SV (order $O(10^{-8})$ *vs* order $O(10^{-6})$ respectively). Furthermore, energy variations ΔE_2 in cases MMP2 and SV2 are four times as big as ΔE_1 of their corresponding counterparts MMP1 and SV1:

$$\Delta E_2(\Delta t_2) = 4\Delta E_1(\Delta t_1), \quad \text{for } \Delta t_2 = 2\Delta t_1, \tag{30}$$

i.e., a quadratic increase of the energy oscillations occurs when doubling the time step, which verifies MMP and SV as second-order schemes in time.

4.4 TC4: Validation against wavetank data

Experiments were conducted in the shallow-water basin of MARIN (cf. test case 202002 in Bunnik (2010)), which includes piston wavemakers and a flat bottom, with a rest depth of $H(x) = H_0 = 1.0\text{m}$, *cf.* Fig. 9. Several wave groups of various steepness were generated in order to generate a focussed wave. Probes were placed at various locations $x_1 = 10\text{m}$, $x_2 = 20\text{m}$, $x_3 = 40\text{m}$, $x_4 = 49.5\text{m}$, $x_5 = 50\text{m}$ and $x_6 = 54\text{m}$ from the wavemaker in order to measure the free-surface elevation. These data as well as the wavemaker motion and velocity were recorded at a frequency of 50Hz and used to initialise and validate

our numerical model in a 2D vertical plane or cross-section, cf. Gagarina et al. (2014). The objective of TC4 is validation of wave-tank measurements of driven waves in a numerical set-up that employs the actual piston wavemaker motion.

Figure 9. TC4: schematic of MARIN's wave basin. The tank is 195.4m long, with a constant water depth at rest of 1.0m. A piston-type wavemaker oscillates sinusoidally with mean position $x = 0$m and generates the waves.

4.4.1 Importing data from measurements

In order to generate the same wave spectra as those in the shallow-water basin of MARIN, the measured wavemaker motion and velocity are interpolated linearly and assigned to the corresponding numerical functions at each time step. To meet the CFL condition (12), the time step Δt used in our simulations must be smaller than the one used to record the data, i.e. $\Delta t_{data} = 1/50$s. To use the measured wavemaker motion and velocity at each time step, we interpolate them with first-order polynomials in each measured time interval $[t_1, t_2]$. Therefore, at time t, the interpolated motion $R_{int}(t)$ and velocity $u_{int}(t)$ of the measured motion R_{dat} and measured velocity u_{dat} are obtained as follows

$$R_{int}(t) = \frac{(t-t_1)R_{dat}(t_2) - (t-t_2)R_{dat}(t_1)}{t_2 - t_1} \quad \text{and}$$
$$u_{int}(t) = \frac{(t-t_1)u_{dat}(t_2) - (t-t_2)u_{dat}(t_1)}{t_2 - t_1}. \tag{31}$$

The interpolations (31) are updated in time and assigned to the wavemaker motion and velocity functions. Note that in this 2D case there is no y-dependence in the wavemaker motion: $\partial_y R = 0$. Fig. 10 shows that the interpolated motion and velocity of the wavemaker agrees with the measurements to a degree that is visually indistinguishable on the presented scale (i.e., with approximately 10^{-3} relative error). The numerical free-surface elevation resulting from this wavemaker input signal may then be saved and compared to the experimental data. Simulations are analysed next.

4.4.2 Focussed wave: dispersion effects

The wavemaker input is used to simulate a focussed wave. The wavemaker starts at rest and oscillates with varying amplitude and anharmonic frequencies (*cf.* Fig. 10). Due to dispersion, the waves generated later are longer and hence travel faster than the first waves, such that waves focus at a specific position. In order to capture this wave focussing, probes are placed around a target area near $x = 49.5$m and $x = 50$m.

We consider a 100m-long computational basin with flat seabed $b(x, y) = 0$ and rest water depth $H(x, y) = H_0 = 1.0$m. A fast Fourier transform of the measured wave signals (cf. Fig. 13) shows that the maximal relevant frequency is about $\omega \approx 18$rad/s. The shortest wavelength may be estimated from the linear dispersion relation (14c) to be $k = 2\pi/\lambda$, leading to $\lambda \approx 0.19$m.

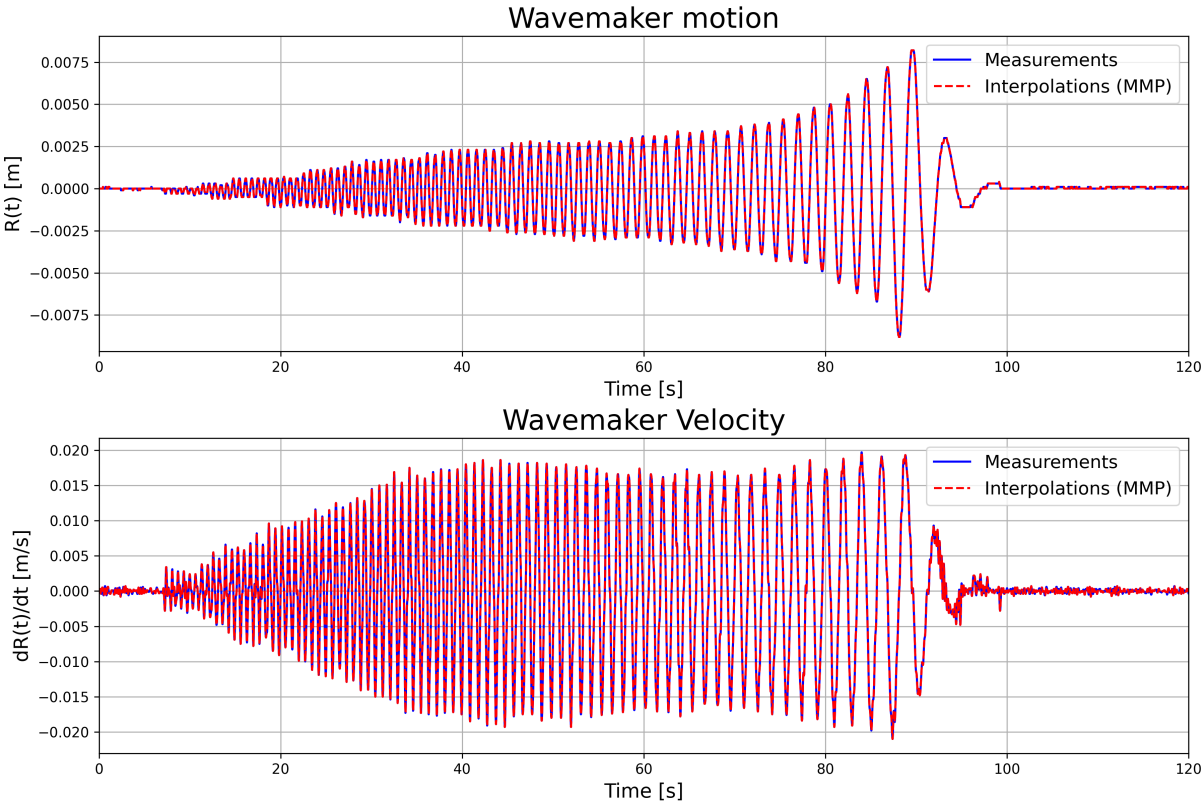

Figure 10. TC4: Interpolated and measured wavemaker motion (top) and velocity (bottom) in the case of focussed wave generation.

Hence, from (12) stability requires that $\Delta x \leq \lambda$, so that the full length of the wave can be resolved by the mesh. However, to ensure accurate results, the wavelength should be evaluated over more than one finite element. To increase numerical accuracy, the mesh resolution is set to $\Delta x = \min(\lambda/20) = 0.01$m for CG1 ($\Delta x = 0.02$ for CG2) and, as a consequence, the time step must satisfy

$$\Delta t_c \leq \frac{2}{\sqrt{g(2\pi/\Delta x)\tanh(2\pi H_0/\Delta x)}} = 0.025\text{s}. \tag{32}$$

To increase accuracy, we set $\Delta t = \Delta t_c/20 = 0.001$s, cf. the time step used in Gagarina et al. (2014). Finally, the vertical resolution over one element is set to GLL-CG9, corresponding to nine horizontal layers ($\Delta z \approx 0.125$m).

Fig. 11 schematically shows the formation of the focussed wave based on a temporal series of representative free-surface profiles using a symplectic-Euler time-stepping scheme, which yields the same results Gidel (2018); Bokhove (2022). First, from $t_0 = 0.0$s to $t_1 = 93.02$s, waves with increasing length and amplitude are generated. At time $t_2 = 105.12$s, it is evident that the waves are closer to each other than when initially generated: dispersion causes the longer waves to travel faster than the shorter ones. At time $t_3 = 109.40$s, the longest waves have caught up with the first, shorter ones, forming a "freak wave" whose amplitude is more than five times higher than waves generated at the early stage of the experiment. Immediately after

time t_3, the longest, fastest waves overtake the shortest ones (*e.g.* at times $t_4 = 113.68$s and $t_5 = 119.98$s), and the waves split again, leading to a mirror-configuration relative to the focussed wave, *i.e.*, compare the snapshot at time t_2 with the one at time t_4.

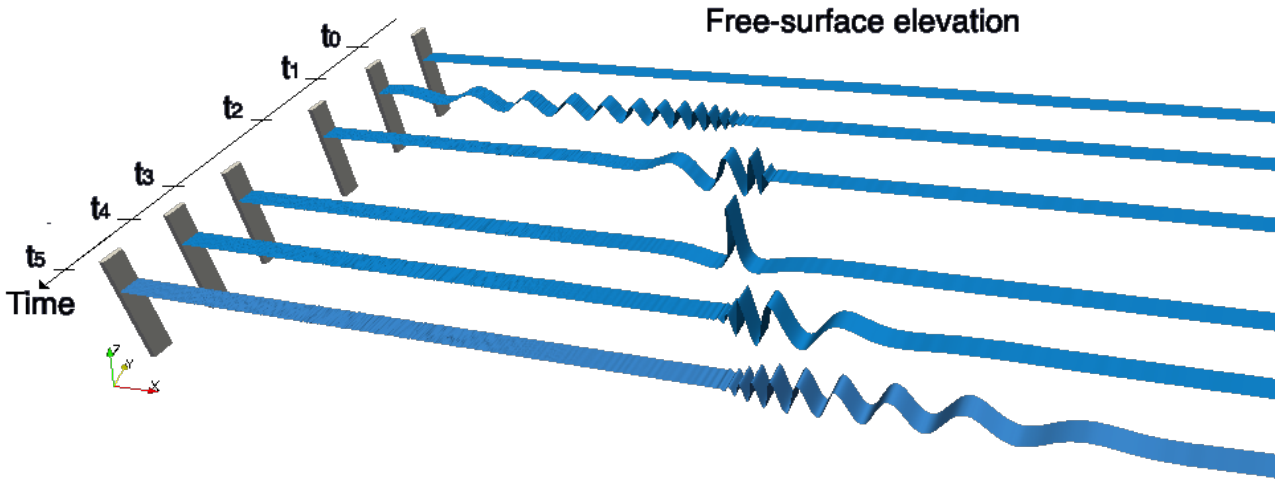

Figure 11. TC4: Temporal snapshots of the free-surface elevation, each rendered as a 3D ribbon, at times $t_0 = 0.0$s, $t_1 = 93.01$s, $t_2 = 105.12$s, $t_3 = 109.40$s, $t_4 = 113.68$s and $t_5 = 119.98$s. The focussed wave is captured at time $t_3 = 109.40$s, whereafter the wave is defocussing again.

Fig. 12 compares the measured (red) time evolution of the wave elevation at the probes with the numerical evolution obtained for the modified-midpoint (dark blue) and Störmer-Verlet (cyan) CG2 schemes. The CG1 and CG2 schemes used give in essence the same results. Both schemes agree reasonably well with the measurements. The freak-wave phase and location agree with the measurements for simulated waves in a target area at least 50m from the wavemaker. Using frequency spectra, Fig. 13 shows that all the experimental modes are well-captured by the present numerical model. In addition, numerical results obtained from the modified-midpoint scheme agree well with those in Gagarina et al. (2014), as demonstrated in Fig. 13. To summarise, the validation of our NWT with the experimental data is successful.

4.5 TC5: Two-soliton interactions with fourfold amplification

In the previous sections, we considered water wave simulations driven by wave makers. A long time after water waves are generated by a wave maker, the waves may travel and interact with each other in an open domain. In this test case, we consider simulations of interacting nonlinear traveling waves or solitons.

The situation is as follows. There are two line solitons with equal amplitude A in the far field $y \to \infty$ and $x \mp \infty$. They lead to an interaction resulting in a line soliton parallel to the y-axis, with a fourfold amplitude $4A$ for a certain optimal angle between the two far-field line-solitons with $y \to \infty$. Such a Y-shaped travelling-soliton-complex can be derived by an exact

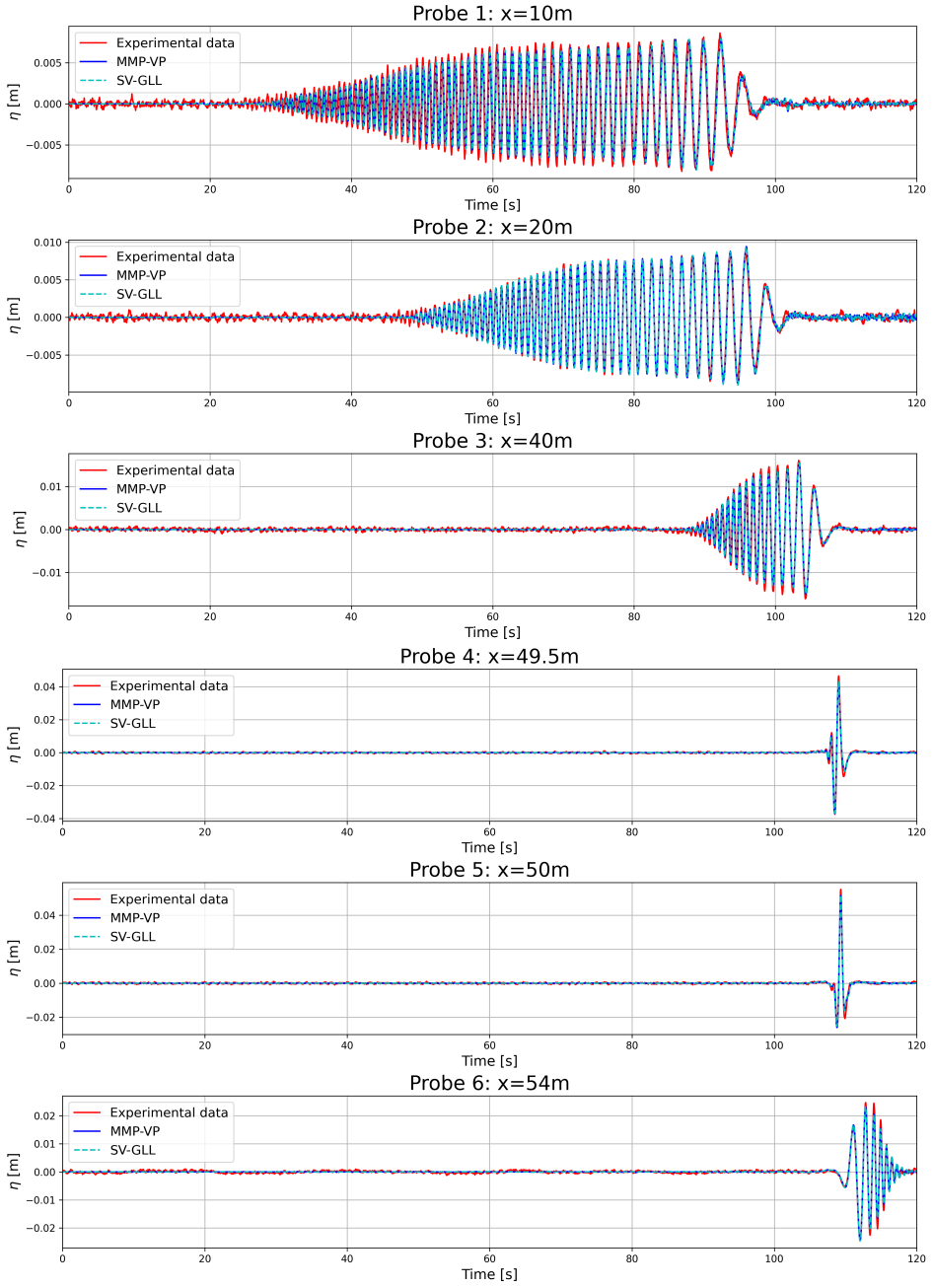

Figure 12. TC4: wave elevations of numerical (blue and cyan) and experimental (red) data at various locations. Numerical results are obtained with modified-midpoint (blue continuous line) and Störmer-Verlet (cyan dashed line) CG2-schemes.

solution of the Kadomtsev-Petviashvili equation (KPE, Kadomtsev and Petviashvili (1970)). To accommodate simulation in

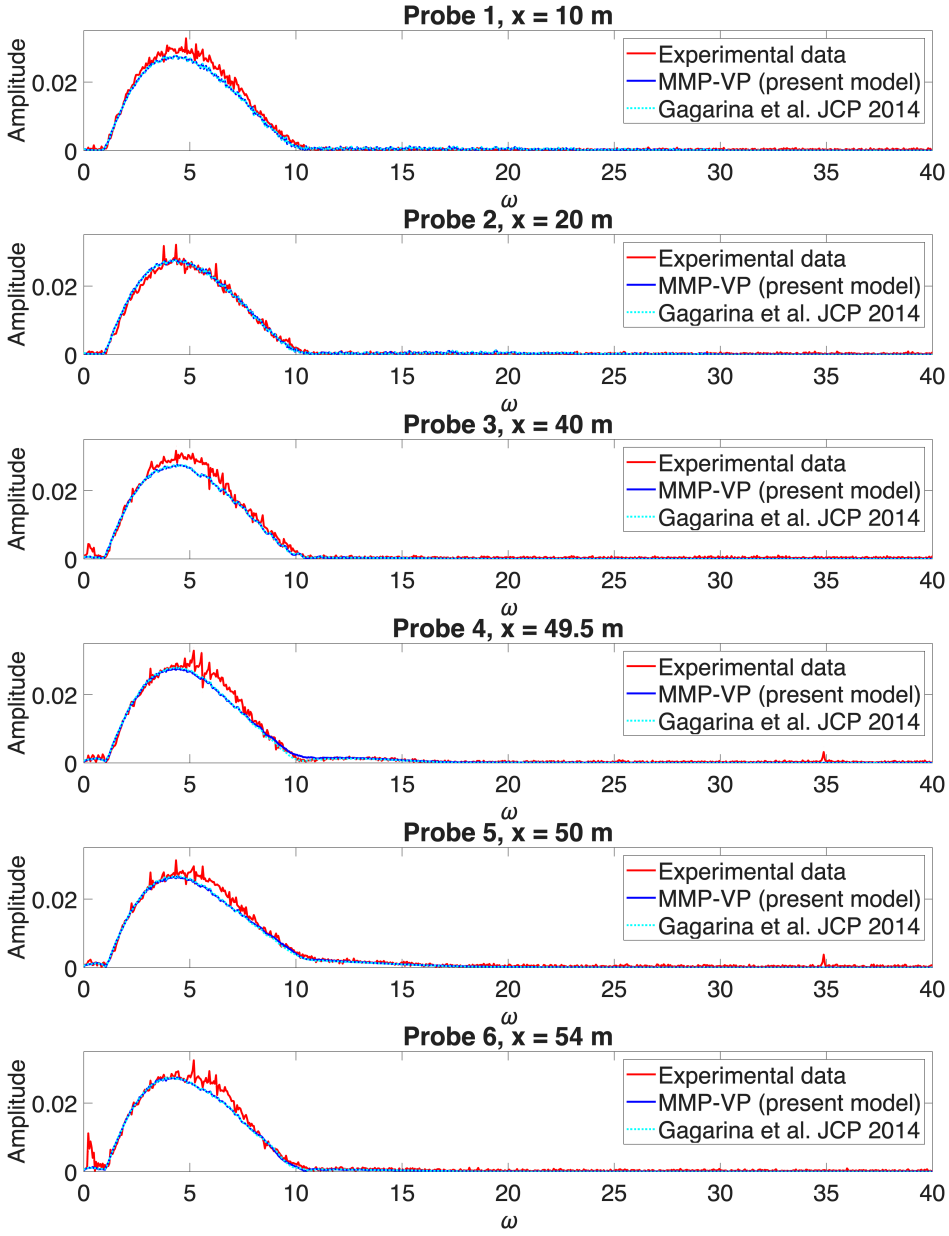

Figure 13. TC4: fast Fourier transform of the wave elevations of numerical (blue and cyan) and experimental (red) data at various locations. Numerical results including these obtained from the present model with modified-midpoint CG2 scheme (blue continuous line) and others from the same test performed in Gagarina et al. (2014) (cyan dashed-dotted line). Corresponding results based on the Störmer-Verlet (CG1 and CG2) scheme are quantitatively similar (see also Lu (2025)).

an x-periodic domain without discontinuous derivatives at that boundary, we have derived an extended λ-Y-soliton solution to the KPE in Appendix B.

Kodama (2010) and others have derived and analysed such exact solutions of the KPE, which is a unidirectional wave equation with weak dependence on the lateral y-direction. This asymptotics is valid in terms of a nonlinearity parameter $\epsilon = a/H_0$ and dispersion parameter $\mu = (H_0/\lambda)^2 = \epsilon^2$, wherein a and λ are typical wave amplitude and wavelength estimates. The question addressed here is whether such fourfold amplification of two interacting solitons, as observed in the KPE, can persist and exist in the more realistic bidirectional PFE. That question has been assessed numerically for the bidirectional Benney-Luke equations (BLE) in Ablowitz and Curtis (2013); Gidel et al. (2017); Choi et al. (2022), with amplifications ranging from 3.6 to 3.9. Here, we present simulations of the potential-flow equations seeded with an exact travelling-wave solution for the KPE, extended into three dimensions by using the expansions underlying the derivation of the BLE from the potential-flow equations.

Details of the computational procedure can be found in Choi et al. (2022), yet we provide a brief summary and present the numerical results next. This well-known Y-soliton solution of the KPE is expressed in transformed, dimensionless coordinates X, Y, τ, which are related to the dimensional x, y, z, t-coordinates via passing through the dimensionless $\hat{x}, \hat{y}, \hat{t}$-coordinates used in the BLE. Their connections read

$$X = \sqrt{\frac{\epsilon}{\mu}} \left(\frac{3}{\sqrt{2}}\right)^{1/3} (\widehat{x} - \widehat{t}) = \frac{\sqrt{\epsilon}}{H_0} \left(\frac{3}{\sqrt{2}}\right)^{1/3} \left(x - \sqrt{gH_0}t\right), \tag{33a}$$

$$Y = \frac{\epsilon}{\sqrt{\mu}} \left(\frac{3}{\sqrt{2}}\right)^{2/3} \widehat{y} = \frac{\epsilon}{H_0} \left(\frac{3}{\sqrt{2}}\right)^{2/3} y, \tag{33b}$$

$$\hat{z} = \frac{z}{H_0}, \quad \tau = \epsilon \sqrt{\frac{2\epsilon}{\mu}} \widehat{t} = \epsilon \sqrt{2\epsilon} \sqrt{\frac{g}{H_0}} t. \tag{33c}$$

The KPE is an equation in terms of a scaled free-surface deviation $u(X, Y, \tau) = 2\partial_{XX} \ln K$ related to a function $K(X, Y, \tau)$, which specification yields the asymptotic solution for the fields ϕ and $h = H_0 + \eta$ in the potential-flow system. Given K, the relevant expressions then become

$$\eta(x, y, t) = \epsilon H_0 \hat{\eta} = 2\epsilon H_0 \left(\frac{4}{3}\right)^{\frac{1}{3}} u = 2\epsilon H_0 \left(\frac{4}{3}\right)^{\frac{1}{3}} \left(\frac{K_{XX}}{K} - \frac{K_X^2}{K^2}\right) \tag{34a}$$

$$\phi(x, y, z, t) = \frac{\epsilon H_0 \sqrt{gH_0}}{\sqrt{\mu}} \sqrt{\epsilon} \left(\frac{4\sqrt{2}}{9}\right)^{1/3} \left(\frac{2K_X}{K} - \frac{1}{2}\mu \frac{z^2}{H_0^2} \nabla_{\hat{x}\hat{y}}^2 \left(\frac{2K_X}{K}\right)\right) \tag{34b}$$

$$\nabla_{\hat{x}\hat{y}}^2 = \left(\frac{\epsilon}{\mu} \left(\frac{3}{\sqrt{2}}\right)^{2/3} \partial_{XX} + \frac{\epsilon^2}{\mu} \left(\frac{3}{\sqrt{2}}\right)^{4/3} \partial_{YY}\right) \left(\frac{2K_X}{K}\right) \tag{34c}$$

$$\partial_{XX} \left(\frac{2K_X}{K}\right) = 2\left(\frac{K_{XXX}}{K} - 3\frac{K_{XX}K_X}{K^2} + 2\frac{K_X^3}{K^3}\right) \tag{34d}$$

$$\partial_{YY} \left(\frac{2K_x}{K}\right) = 2\left(\frac{K_{XYY}}{K} - 2\frac{K_{XY}K_Y}{K^2} - \frac{K_X K_{YY}}{K^2} + 2\frac{K_X K_Y^2}{K^3}\right), \tag{34e}$$

which are used to initialise the potential-flow equations at the free surface, i.e. for $\eta(x, y, 0)$ and $\phi(x, y, H_0 + \eta(x, y, 0), 0)$, at time $t = 0$. We refer to Kodama (Kodama, 2010; Choi et al., 2022) for the two-soliton expression of $K(X, Y, \tau)$ (or to the provided codes).

To implement matters, two subtleties need to be overcome. First, the two-soliton solution for the KPE holds on an infinite horizontal plane and we limit this approximately to an x-periodic channel geometry using the symmetry of the solution. This procedure yields (minor) errors in the top corner of the domain away from the interaction region. However, the solution for the velocity potential is not periodic in x. Hence, a partition of the velocity potential is needed as follows

$$\phi(x,y,z,t) = U_0(y,z)x + \tilde{\phi}(x,y,z,t) \tag{35a}$$

with

$$U_0(y,z) = \frac{\phi_0(x_2,y,z) - \phi_0(x_1,y,z)}{x_2 - x_1}, \tag{35b}$$

in a suitably chosen x-periodic domain $x \in [x_1, x_2], y \in [y_1, y_2]$ and $\phi_0 = \phi(x,y,z,0)$, such that $\tilde{\phi}$ becomes periodic. Second, these expressions need to be transformed to the fixed, computational domain, in which process another approximation has been made. Since we have no wavemaker in this case, the only transformation is $z = \hat{z}h(\hat{x},\hat{y},\hat{t})/H_0$, which greatly simplifies the (time-discrete) VP involved.

In the transformed coordinates, the time-discrete modified-midpoint VP emerges, as follows and in which the hats have been omitted,

$$\begin{aligned}
0 = \delta \int_{x_1}^{x_2}\int_{y_1}^{y_2} \psi^{n+1/2}\frac{(h^{n+1}-h^n)}{\Delta t} - h^{n+1/2}\frac{(\psi^{n+1}-\psi^n)}{\Delta t} - \frac{1}{2}g(h^{n+1/2})^2 + gh^{n+1/2}H_0 \,\mathrm{d}x\,\mathrm{d}y \\
- \int_{x_1}^{x_2}\int_{y_1}^{y_2}\int_0^{H_0} \frac{1}{2}\frac{h^{n+1/2}}{H_0}\left(U_0 + \hat{\phi}\partial_x\psi^{n+1/2} + \partial_x\varphi^{n+1/2} - \frac{z}{h^{n+1/2}}\partial_x h^{n+1/2}(\psi^{n+1/2}\partial_z\hat{\phi} + \partial_z\varphi^{n+1/2})\right)^2 \\
+ \frac{1}{2}\frac{h^{n+1/2}}{H_0}\left(x\partial_y U_0 + \hat{\phi}\partial_y\psi^{n+1/2} + \partial_y\varphi^{n+1/2} - \frac{z}{h^{n+1/2}}\partial_y h^{n+1/2}(\underline{x\partial_z U_0} + \psi^{n+1/2}\partial_z\hat{\phi} + \partial_z\varphi^{n+1/2})\right)^2 \\
+ \frac{1}{2}\frac{H_0}{h^{n+1/2}}\left(x\partial_z U_0 + \psi^{n+1/2}\partial_z\hat{\phi} + \partial_z\varphi^{n+1/2}\right)^2 \mathrm{d}z\,\mathrm{d}x\,\mathrm{d}y
\end{aligned} \tag{36a}$$

together with

$$\psi^{n+1} = 2\psi^{n+1/2} - \psi^n, \qquad h^{n+1} = 2h^{n+1/2} - h^n. \tag{36b}$$

However, in the current numerical implementation, we have used a second approximation, i.e.

$$U_0 = U_0(y, zh/H_0) \approx U_0(y,z), \tag{37}$$

in which z is the transformed coordinate. Note that (36) is a simplified version of (10) for an x-periodic domain.

Finally, the above set-up made it possible to conduct four simulations using the two-soliton solution (B1) as initial condition, while varying the time step and spatial resolutions. Two basis functions have been used: second-order and fourth-order Gauss-Lobatto-Legendre polynomials, denoted by CG2 and CG4. In detail, the four simulations have been conducted using four cases of spatial-temporal resolutions: a) (CG2,$\Delta x = \Delta y$,Δt), b) (CG4,$2\Delta x = 2\Delta y$,Δt), c) (CG2,$\Delta x/2 = \Delta y/2$,Δt), and d)

(CG2,$\Delta x = \Delta y$,$\Delta t/2$) where the basic spatial and temporal mesh size are $\Delta x = 965.4/97$ and $\Delta t = 0.2856$, respectively. The two-soliton parameter values used are provided in the table within Fig 14.

Simulation data are given in the table within Fig 15, including run times. The initial conditions and final fields shown in Fig. 14 reveal the periodicity of the perturbation velocity potential $\tilde{\phi}$ as well as the amplification sustained. Further simulation results are summarised in Fig. 15. All simulations appear to be stable, as can be discerned from the energy plot in Fig. 15(b), which demonstrates second-order accuracy in time. The CG2-simulation with time step $\Delta t/2$ shows the expected fourfold reduction. The maximum amplification is established by the ratio of the maximum amplitude over the far-field amplitude versus time, see Fig. 15(c,d), and straddles eventually between circa 3.9 and 4.1. Recall that the exact KPE-solution has a fixed fourfold amplification. Hence, the set of simulations together demonstrate the robustness of the results. It took some computational efforts to attain the spatial-temporal resolution required to successfully simulate the approximately fourfold amplification in this two-soliton travelling solution with the potential-flow equations. To conclude, compared to simulations with the more well-known Y-shaped solitons as initial seed (Ablowitz and Curtis, 2013; Gidel et al., 2017; Choi et al., 2022, 2024), these x-periodic simulations with the λ–Y-shaped solitons are much better behaved and surprisingly non-dispersive.

5 Summary with discussion

A novel fully space-time methodology based on the main governing time-discrete variational principle has been developed for the modelling and subsequent computational solution of 3D nonlinear potential-flow water-wave problems. The three goals defined at the onset have largely been reached, in turn:

- A space-time variational spectrally-accurate finite-element model of 3D potential-flow dynamics based on deriving consistent weak forms from a space-discrete variational principle (VP) was established. More importantly, we developed a space-time discrete VP from which the algebraically cumbersome weak forms have been derived automatically within the finite-element environment *Firedrake*. In both cases, higher-order and spectral spatial accuracy can be chosen prior to a simulation, with possibly different h and p resolution in the horizontal and vertical. The advantages of the VP-approach are the reduction of development time and human errors as well as the scope it thus has to readily combine potential-flow dynamics with structural dynamics in FSI and wave-energy devices (cf. Salwa et al. (2017b); Bolton et al. (2021)).

- Within this VP-discretisation we consistently embedded the non-autonomous driving of waves by wavemakers with prescribed motion $x = R(y,t)$ on one side of the wave-basin, meaning that for each y-location the wavemaker is a "piston" but these piston-motions can smoothly vary in y. Such consistency was achieved by turning the non-autonomous or explicit-time dependence into an implicit time-dependence within the (time-discrete) VP.

- Finally, a series of five test cases provided a first set of verification and validation examples of this VP-based discretisation, including a new error analysis, a validation against (open) 2D (vertical cross-section) experimental data as well as a novel two-soliton amplification solution in 3D. A three-soliton test case with nine-fold wave-amplification (dubbed test

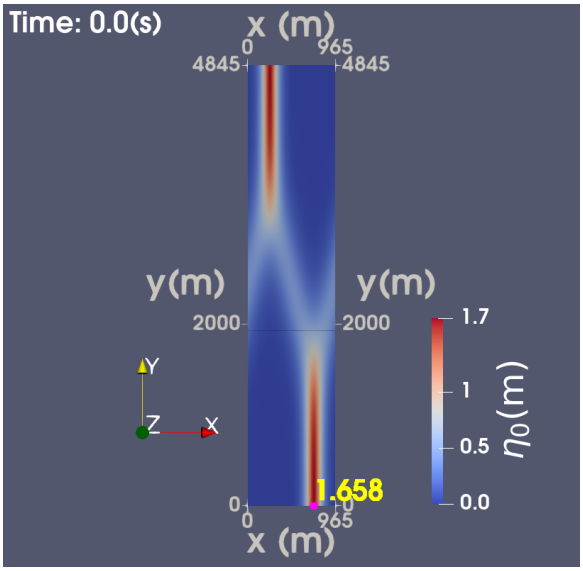

(a) Initial condition for η_0

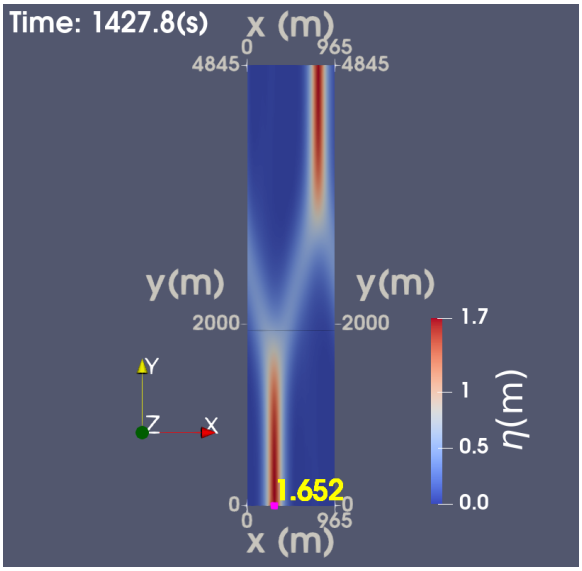

(b) η at $t_{end} = 1427.8$

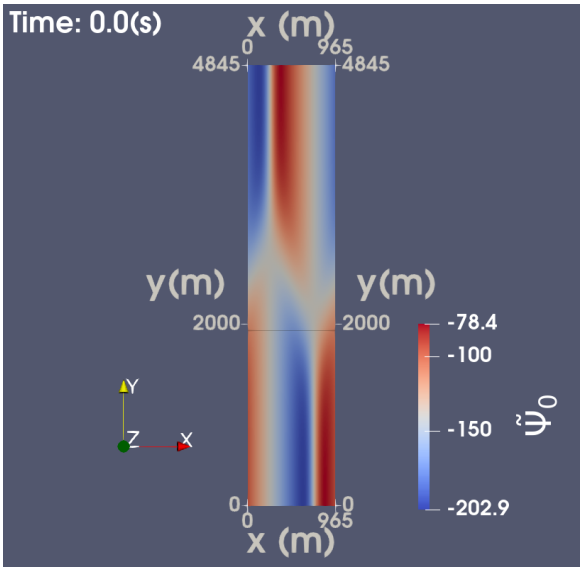

(c) Initial condition for $\tilde{\psi}_0$

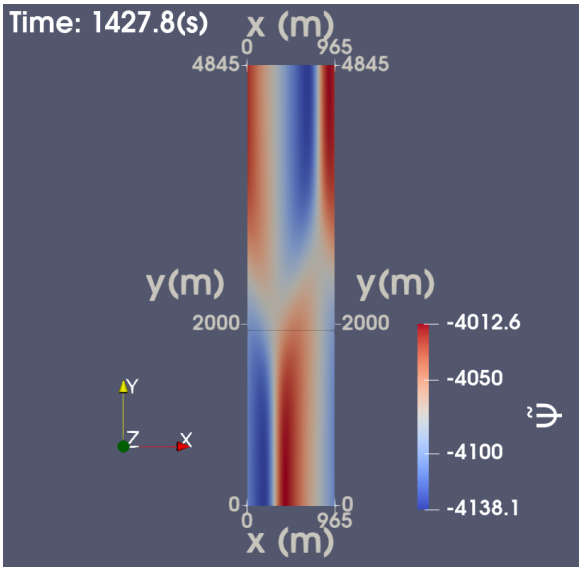

(d) $\tilde{\psi}$ at $t_{end} = 1427.8$

Parameters	ϵ	μ	Y_0	τ_0	δ	k_1	k_2	k_3	k_4
PFE-TC5	0.05	ϵ^2	3	0	10^{-5}	$-\sqrt{\frac{5}{6}\left(\frac{3}{4}\right)^{1/3}}$	$k_1 + \delta$	δ	$-k_1$

Figure 14. TC5: Initial conditions for (a) η_0 and (c) $\tilde{\psi}$ in the PFE-TC5 simulation with $\epsilon = 0.05$, with polynomials of order CG2 and time step $\Delta t = 0.2856$s. Panel (b) and (d) show numerical solutions at $t_{end} = 1427.8$s. Axes and η have units of m, time has unit s and ϕ of m^2/s. These settings for k_i yield $A = 0.4166$m and $\max(\eta_0) = 4A = 1.666$m with width ~ 200m for a depth of $H_0 = 20$m. The fourfold soliton then has an amplitude of circa 1.6m across 400m. Yellow larger values near the bottom in the η-snapshots denote the maximum.

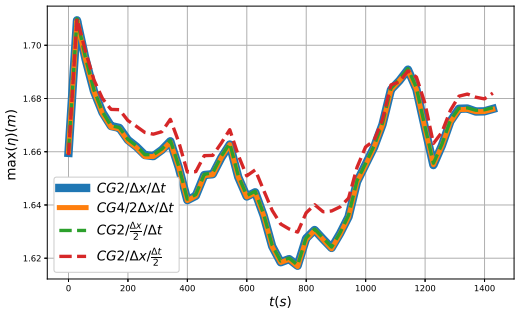

(a) Maximum values of η

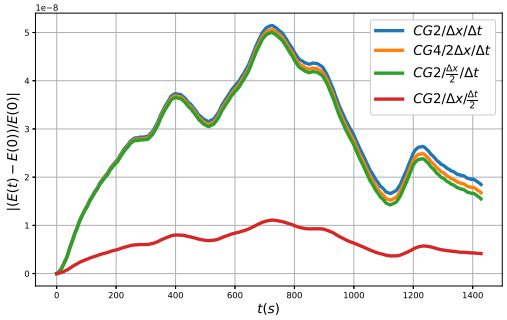

(b) Relative energy

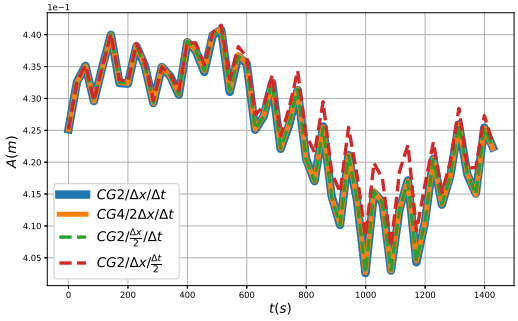

(c) A over time

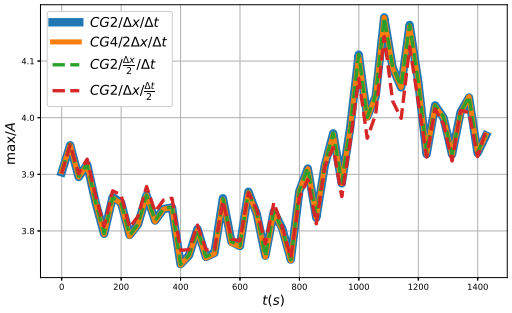

(d) $\max(\eta)/A$ against time

Figure 15. TC5: Results from four potential-flow dynamics simulations seeded with two-soliton interactions (B1). We carried out four simulations varying spatial-temporal resolutions: a. (CG2,$\Delta x = \Delta y$,Δt) (the blue solid line), b. (CG4,$2\Delta x = 2\Delta y$,Δt) (the orange solid line), c. (CG2,$\Delta x/2 = \Delta y/2$,Δt) (the green dashed line), and d. (CG2,$\Delta x = \Delta y$,$\Delta t/2$) (the red dashed line) where the basic spatial and temporal mesh size are $\Delta x = 965.4/97$ and $\Delta t = 0.2856$, respectively. Shown are: (a) Maximum values of η over time. (b) Relative energy error $|1 - E(t)/E(0)|$ in time with $E(0) = -1.8335 \times 10^{11}$ for $CG2$ and $CG4$ (up to six digits). (c) $A := \max_x(\eta(\cdot, y = 2500, t))$. (d) The amplification displayed as maximum value of η divided by A over time.

Simulation	L_x (m)	L_y (m)	$L_z = H_0$ (m)	T (s)	Δt_{BLE}	N_x	N_y	N_z	DoFs	Run time (min)
PFE: CG2/$\Delta x/\Delta t$	965.4	4845.7	20	1428.0	0.01	97	485	4	1,695,366	615
PFE: CG4/2$\Delta x/\Delta t$	965.4	4845.7	20	1428.0	0.01	48	242	4	1,674,432	1066
PFE: CG2/$\frac{\Delta x}{2}/\Delta t$	965.4	4845.7	20	1428.0	0.01	193	969	4	6,736,086	3409
PFE: CG2/$\Delta x/\frac{\Delta t}{2}$	965.4	4845.7	20	1428.0	0.005	97	485	4	1,695,366	1276

case TC6) of the VP-discretisation has been demonstrated elsewhere, in Choi et al. (2024). These test cases are openly accessible via *Firedrake* and *GitHiub* and provide a platform for the inclusion of other test cases.

The above developments are novel in that these provide the first fully space-time discrete VP-based discretisations in 3D with higher-order spectral spatial accuracy and variational consistency in time. Furthermore, all mathematical-numerical algorithms have been implemented as open access codes within the open-access *Firedrake* environment. It is useful to stress the difference of developing implementations of new algorithms within a finite-element environment such as *Firedrake* (or in a finite-difference or spectral environment such as "*Dedalus*" (Burns et al., 2020)), as exemplified by our space-time discrete VP-approach presented, versus the development of a bespoke special-purpose code for a specific set of PDEs. Reduction of development time, ease of implementation, use of (spectral) higher-order polynomials and parallel computing in the former are juxtaposed against special-purpose development, less-accessible intricacies and most-likely best performance in the latter. Further research is underway to advance the solver parameters of the in-built Firedrake solvers, which will then be generically accessible for a suite of water-wave and FSI applications. We make the case that both developments have their merits.

Finally, in a sequel to the VP-based finite-element approach presented here we have included wave-absorption at a shallow beach at one end of the wave basin. Herein, wave-absorption has been implemented in the numerical algorithm by coupling the potential-flow dynamics in deeper waters to shallow-water dynamics with hydraulic bores at the beach. The finite-element approach presented here is used for the potential-flow dynamics in deeper waters and a finite-volume method allows dissipation in hydraulic bores for the shallow-water dynamics. Again fluxes at a judiciously chosen coupling point between the models (in a vertical 2D cross-section) are derived by considering VPs, for both potential-flow and shallow-water dynamics. Expositions of these wave-beach simulations, including validation against bespoke experimental data, can be found in detail in Gidel as well as Lu (Gidel, 2018; Lu, 2025) with an overview by Bokhove (2022).

Code availability. Codes used, run times and corresponding simulation instructions, ensuring reproducibility, cf. Ritchie (2021), can be found at Zenodo https://doi.org/10.5281/zenodo.16919659, see Bokhove (2025).
See also. https://github.com/obokhove/TCs3Dnumericalwavetank2022ff/releases/tag/NWTPFv1.0.0
and https://github.com/obokhove/TCs3Dnumericalwavetank2022ff

Video supplement. Zoom-in of test case TC4 "202002_zoom_splash.avi": https://www.youtube.com/watch?v=L_ENnHuTSGc

Appendix A: Coordinate transformation

The Jacobian of transforms (4) mapping (x, y, z, t) to $(\hat{x}, \hat{y}, \hat{z}, \hat{t})$ is, after substitution of all *explicit* occurrences of x, y, z and t,

$$J \equiv \frac{\partial(\hat{x}, \hat{y}, \hat{z}, \hat{t})}{\partial(x, y, z, t)} = \begin{bmatrix} \dfrac{L_w}{L_w - \tilde{R}} & \dfrac{(\hat{x} - L_w)\tilde{R}_y}{L_w - \tilde{R}} & 0 & \dfrac{(\hat{x} - L_w)\tilde{R}_t}{L_w - \tilde{R}} \\ 0 & 1 & 0 & 0 \\ -\dfrac{\hat{z}h_x + H_0 b_x}{h} & -\dfrac{\hat{z}h_y + H_0 b_y}{h} & \dfrac{H_0}{h} & -\dfrac{\hat{z}h_t}{h} \\ 0 & 0 & 0 & 1 \end{bmatrix}, \tag{A1}$$

in which partial derivatives with respect to x, y, t must now be expressed explicitly in terms of transformed variables. To this end, first note that the inverse

$$\hat{J} \equiv \frac{\partial(x, y, z, t)}{\partial(\hat{x}, \hat{y}, \hat{z}, \hat{t})}$$

of J is computed directly from (A1) as

$$\hat{J} = \begin{bmatrix} \dfrac{L_w - \tilde{R}}{L_w} & -\dfrac{(\hat{x} - L_w)\tilde{R}_y}{L_w} & 0 & -\dfrac{(\hat{x} - L_w)\tilde{R}_t}{L_w} \\ 0 & 1 & 0 & 0 \\ \dfrac{(\hat{z}h_x + H_0 b_x)(L_w - \tilde{R})}{L_w H_0} & \dfrac{\hat{z}h_y}{H_0} + b_y - \dfrac{(\hat{z}h_x + H_0 b_x)(\hat{x} - L_w)\tilde{R}_y}{L_w H_0} & \dfrac{h}{H_0} & \dfrac{\hat{z}h_t}{H_0} - \dfrac{(\hat{z}h_x + H_0 b_x)(\hat{x} - L_w)\tilde{R}_t}{L_w H_0} \\ 0 & 0 & 0 & 1 \end{bmatrix}, \tag{A2}$$

whence the chain rule and (A2) give

$$\begin{bmatrix} b_{\hat{z}} \\ h_{\hat{z}} \\ \tilde{R}_{\hat{z}} \end{bmatrix} = \underline{\underline{\hat{J}_{1,3}}} \begin{bmatrix} b_x \\ h_x \\ \tilde{R}_x \end{bmatrix} + \underline{\underline{\hat{J}_{2,3}}} \begin{bmatrix} b_y \\ h_y \\ \tilde{R}_y \end{bmatrix} + \hat{J}_{3,3} \begin{bmatrix} \underline{b_z} \\ \underline{h_z} \\ \underline{\tilde{R}_z} \end{bmatrix} + \underline{\underline{\hat{J}_{4,3}}} \begin{bmatrix} \underline{b_t} \\ h_t \\ \tilde{R}_t \end{bmatrix} = \begin{bmatrix} 0 \\ 0 \\ 0 \end{bmatrix}. \tag{A3}$$

in which singly and doubly underlined terms vanish by (4) and (A2) respectively. Applying the chain rule once again now gives

$$\begin{bmatrix}\tilde{R}_y\\ \tilde{R}_t\end{bmatrix} = \begin{bmatrix}J_{1,2}\\ J_{1,4}\end{bmatrix}\underline{\tilde{R}_{\hat{x}}} + \begin{bmatrix}J_{2,2}\\ \underline{\underline{J_{2,4}}}\end{bmatrix}\tilde{R}_{\hat{y}} + \begin{bmatrix}J_{3,2}\\ J_{3,4}\end{bmatrix}\underline{\underline{\tilde{R}_{\hat{z}}}} + \begin{bmatrix}\underline{\underline{J_{4,2}}}\\ J_{4,4}\end{bmatrix}\tilde{R}_{\hat{t}} = \begin{bmatrix}1\\ 0\end{bmatrix}\tilde{R}_{\hat{y}} + \begin{bmatrix}0\\ 1\end{bmatrix}\tilde{R}_{\hat{t}} = \begin{bmatrix}\tilde{R}_{\hat{y}}\\ \tilde{R}_{\hat{t}}\end{bmatrix}, \tag{A4a}$$

$$\begin{bmatrix}b_x\\ b_y\end{bmatrix} = \begin{bmatrix}J_{1,1}\\ J_{1,2}\end{bmatrix}b_{\hat{x}} + \begin{bmatrix}\underline{\underline{J_{2,1}}}\\ J_{2,2}\end{bmatrix}b_{\hat{y}} + \begin{bmatrix}J_{3,1}\\ J_{3,2}\end{bmatrix}\underline{\underline{b_{\hat{z}}}} + \begin{bmatrix}\underline{\underline{J_{4,1}}}\\ \underline{\underline{J_{4,2}}}\end{bmatrix}\underline{b_{\hat{t}}} = \frac{1}{\hat{W}}\begin{bmatrix}L_w\\ \hat{U}\end{bmatrix}b_{\hat{x}} + \begin{bmatrix}0\\ 1\end{bmatrix}b_{\hat{y}}, \tag{A4b}$$

$$\begin{aligned}\begin{bmatrix}h_x\\ h_y\\ h_t\end{bmatrix} &= \begin{bmatrix}J_{1,1}\\ J_{1,2}\\ J_{1,4}\end{bmatrix}h_{\hat{x}} + \begin{bmatrix}\underline{\underline{J_{2,1}}}\\ J_{2,2}\\ \underline{\underline{J_{2,4}}}\end{bmatrix}h_{\hat{y}} + \begin{bmatrix}J_{3,1}\\ J_{3,2}\\ J_{3,4}\end{bmatrix}\underline{\underline{h_{\hat{z}}}} + \begin{bmatrix}\underline{\underline{J_{4,1}}}\\ \underline{\underline{J_{4,2}}}\\ J_{4,4}\end{bmatrix}h_{\hat{t}}\\ &= \frac{1}{\hat{W}}\begin{bmatrix}L_w\\ \hat{U}\\ \hat{X}\tilde{R}_{\hat{t}}\end{bmatrix}h_{\hat{x}} + \begin{bmatrix}0\\ 1\\ 0\end{bmatrix}h_{\hat{y}} + \begin{bmatrix}0\\ 0\\ 1\end{bmatrix}h_{\hat{t}}\end{aligned} \tag{A4c}$$

in which singly, doubly and triply underlined terms vanish by (4), (A1) and (A3) respectively, and where $\hat{X}$, $\hat{U}$ and $\hat{W}$ are defined in (6), in which hats were hitherto removed for brevity but now resurrected to distinguish between coordinate systems. Substitution of (A4) into (A1) now leads to the fully explicit form of the required Jacobian,

$$J = \begin{bmatrix} \frac{L_w}{\hat{W}} & \frac{\hat{U}}{\hat{W}} & 0 & \frac{\hat{X}}{\hat{W}}\tilde{R}_{\hat{t}} \\ 0 & 1 & 0 & 0 \\ -\frac{L_w}{\hat{W}}\frac{\hat{z}h_{\hat{x}} + H_0 b_{\hat{x}}}{h} & -\frac{\hat{z}}{h}\left(\frac{\hat{U}}{\hat{W}}h_{\hat{x}} + h_{\hat{y}}\right) - \frac{H_0}{h}\left(\frac{\hat{U}}{\hat{W}}b_{\hat{x}} + b_{\hat{y}}\right) & \frac{H_0}{h} & -\frac{\hat{z}}{h}\left(\frac{\hat{X}\tilde{R}_{\hat{t}}}{\hat{W}}h_{\hat{x}} + h_{\hat{t}}\right) \\ 0 & 0 & 0 & 1 \end{bmatrix}, \tag{A5}$$

using which the required transformed partial derivatives of the potential ϕ follow from the chain rule and (A5) as

$$\begin{aligned}\begin{bmatrix}\phi_x\\ \phi_y\\ \phi_z\\ \phi_t\end{bmatrix} &= J^T\begin{bmatrix}\phi_{\hat{x}}\\ \phi_{\hat{y}}\\ \phi_{\hat{z}}\\ \phi_{\hat{t}}\end{bmatrix}\\ &= \frac{1}{\hat{W}}\begin{bmatrix}L_w\\ \hat{U}\\ 0\\ \hat{X}\tilde{R}_{\hat{t}}\end{bmatrix}\phi_{\hat{x}} + \begin{bmatrix}0\\ 1\\ 0\\ 0\end{bmatrix}\phi_{\hat{y}} - \frac{1}{\hat{W}h}\begin{bmatrix}L_w\left(\hat{z}h_{\hat{x}} + H_0 b_{\hat{x}}\right)\\ \hat{U}\left(\hat{z}h_{\hat{x}} + H_0 b_{\hat{x}}\right) + \hat{W}\left(\hat{z}h_{\hat{y}} + H_0 b_{\hat{y}}\right)\\ -\hat{W}H_0\\ \hat{z}\left(\hat{X}\tilde{R}_{\hat{t}}h_{\hat{x}} + \hat{W}h_{\hat{t}}\right)\end{bmatrix}\phi_{\hat{z}} + \begin{bmatrix}0\\ 0\\ 0\\ 1\end{bmatrix}\phi_{\hat{t}}.\end{aligned} \tag{A6}$$

Finally, the spatio-temporal volume element in (2) transforms according to

$$\mathrm{d}x\,\mathrm{d}y\,\mathrm{d}z\,\mathrm{d}t = |\hat{J}|\,\mathrm{d}\hat{x}\,\mathrm{d}\hat{y}\,\mathrm{d}\hat{z}\,\mathrm{d}\hat{t} = \frac{\hat{W}}{L_w}\frac{h}{H_0}\mathrm{d}\hat{x}\,\mathrm{d}\hat{y}\,\mathrm{d}\hat{z}\,\mathrm{d}\hat{t}. \tag{A7}$$

Appendix B: A novel type of two-soliton interactions with fourfold amplification

To create an asymptotically-accurate initial condition for seeding the potential-flow system, we start from the theory of exact solutions for the Kadomtsev-Petviashvili equation (KPE, Kodama (2018)). It is an extension of the classical two-soliton solution with a fourfold amplification, which is more suitable for numerical testing since the far-fields are asymptotically normal to lateral channel walls[2]. The variable $u(X,Y,\tau)$ in the KPE is a non-dimensional scaled version of the deviation $\eta(x,y,t)$ from the rest water-surface level in the potential-flow system. It has dimensionless coordinates X,Y,τ as counterparts. While the solution below is bespoke to this article, for the precise link between $\eta(x,y,t)$ and $u(X,Y,\tau)$ we refer to Choi et al. (2024) and our accessible codes. We note that

$$u(X,Y,\tau) = 2\partial_{XX}\ln K(X,Y,\tau) = 2\frac{K\partial_{XX}K - (\partial_X K)^2}{K^2}, \tag{B1}$$

which function $K(X,Y,\tau)$ we define next. A so-called P-type matrix reads

$$\mathcal{A} = \begin{pmatrix} 1 & 0 & 0 & -b \\ 0 & 1 & a & 0 \end{pmatrix} \tag{B2}$$

with constants $a,b>0$ such that

$$\mathbf{f} = (f_1,f_2)^T = \mathcal{A}(e^{\theta_1},e^{\theta_2},e^{\theta_3},e^{\theta_4})^T \quad \text{yielding} \quad f_1 = e^{\theta_1} - be^{\theta_4}, f_2 = e^{\theta_2} + ae^{\theta_3},$$

wherein $\theta_i = k_iX + k_i^2Y - k_i^3\tau$ with wavenumber k_i and $i=1,2,3,4$. These wavenumbers are ordered as $k_1<k_2<k_3<k_4$. Subsequently, the above defines the introduced function $K(X,Y,\tau)$ as follows

$$K(X,Y,\tau) = f_1\partial_X f_2 - f_2\partial_X f_1 \tag{B3a}$$

$$= (k_2-k_1)e^{\theta_1+\theta_2} + a(k_3-k_1)e^{\theta_1+\theta_3} + b(k_4-k_2)e^{\theta_2+\theta_4} + ab(k_4-k_3)e^{\theta_3+\theta_4} \tag{B3b}$$

$$= a(k_3-k_1)e^{\theta_1}\left(e^{\theta_3} + \frac{k_2-k_1}{a(k_3-k_1)}e^{\theta_2}\right) + ab(k_4-k_3)e^{\theta_4}\left(e^{\theta_3} + \frac{(k_4-k_2)}{a(k_4-k_3)}e^{\theta_2}\right). \tag{B3c}$$

[2]OB was able to construct this so-called Y–λ soliton compound after instructions by and extensive discussion with Prof Yuji Kodama, whose involvement therein we kindly acknowledge.

We can obtain the desired solution via a chord diagram in which $k_1 < 0, k_4 = -k_1$, $k_2 \approx k_1$ and $k_3 \approx 0 = \frac{1}{2}(k_1 + k_4)$ as well as $a = b = 1$. When one picks a value for Y and τ, say $Y_2 = 3$ and $\tau_2 = 0$, one obtains the $X_{1,2}$ locations

$$X_1 = -\frac{\ln\left((k_2 - k_1)/[(k_3 - k_1)a]\right)}{(k_2 - k_3)} - (k_2 + k_3)Y_2 + \frac{k_2^3 - k_3^3}{(k_2 - k_3)}\tau_2 \tag{B4a}$$

$$X_2 = -\frac{\ln\left((k_4 - k_2)/[(k_4 - k_3)a]\right)}{(k_2 - k_3)} - (k_2 + k_3)Y_2 + \frac{k_2^3 - k_3^3}{(k_2 - k_3)}\tau_2 \tag{B4b}$$

$$\Psi = 2\partial_X \ln K = 2\frac{K_X}{K} = U_0 X + \widetilde{\Psi} \tag{B4c}$$

$$U_0 = \frac{\Psi(X_2, Y_2, \tau_2) - \Psi(X_1, Y_2, \tau_2)}{X_2 - X_1}, \tag{B4d}$$

in which $\widetilde{\Psi}$ is X-periodic in $X \in [X_1, X_2]$. We can see that in the $\delta \to 0^+$-limit the $[1,4]$ far-field solitons have a maximum amplification of four times the $[2,3]$ far-field solitons. The $[1,4]$ solitons are nearly aligned in the Y-direction when $Y \to \pm\infty$. This solution of $u(X, Y, \tau)$ and $\widetilde{\Psi}(X, Y, \tau)$ at $\tau = 0$ is shown in Fig. B1.

Author contributions. YL improved and extended all codes, simulations and work of FG, including removal of a mild-slope approximation, speed improvements, the new error-analysis and its validation. YL and OB derived and added automated weak formulations based on space-time discrete variational principles (VPs) with MMP time discretisation. MAK and OB acquired EU funding and supervised. OB derived all space-time discrete VPs, set up and implemented (with JC) TC5 and tested/extended TC1, TC3 and TC4; JC performed its simulations. MAK derived the error analysis, extended by YL with help of Dr Evy Kersalé. All authors contributed to proofreading.

Competing interests. None.

Acknowledgements. FG and YL were funded through EU Marie Curie Fellowships for European Industry Doctorates in the projects "*SurfsUp*" (GA 607596) and "*EAGRE*" (GA 859983). JC was funded via a Sejong Science Fellowship Grant "*Research on approximate hierarchy among abnormal wave models*" (2021R1C1C2008763), by the National Research Foundation of Korea and the Korean government (MSIT). Dr Elena Gagarina kindly provided her Fourier-analysis code and data from her simulations Gagarina et al. (2014). A preliminary version of this work is found in Gidel et al. (2022) using explicit and consistent weak formulations following from the space-discrete VP. It is a great pleasure to acknowledge numerous inspiring discussions with Dr Evy Kersalé.

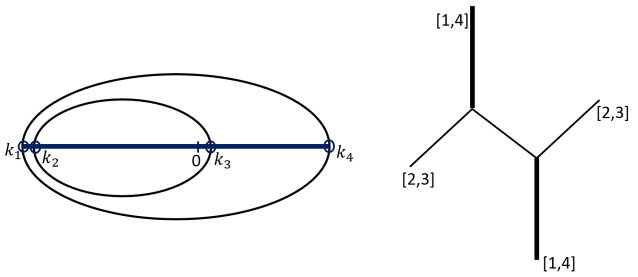

(a) Chord diagram and sketch of soliton branches (based on discussion with Prof Y. Kodama).

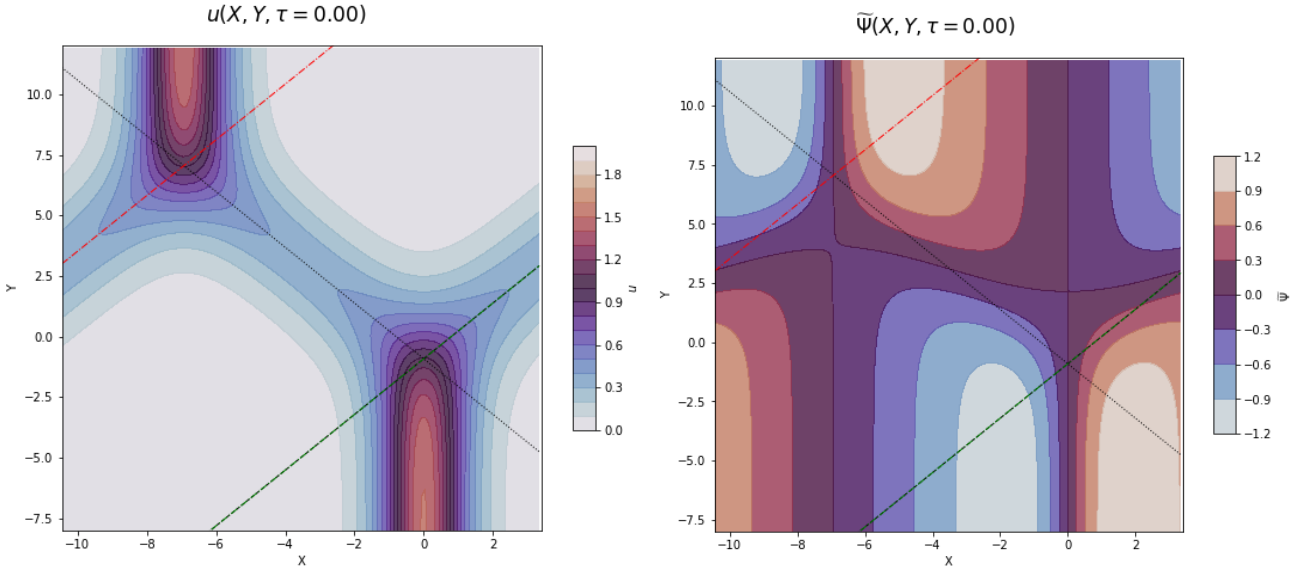

(b) Snapshots of $u(X,Y,\tau)$ and (c) $\widetilde{\Psi}(X,Y,\tau)$ at $\tau = 0$.

Figure B1. (a) Chord-diagram and sketch for a P-type soliton (courtesy Prof. Yuji Kodama). (b,c) Snapshot of a Y–λ soliton solution of the scaled free-surface deviation $u(X,Y,\tau)$ and potential $\widetilde{\Psi}(X,Y,\tau)$ for the Kadomtsev-Petviashvili equation with wavenumber parameter choices $k_1 = -\sqrt{\frac{5}{6}\left(\frac{3}{4}\right)^{1/3}}, k_2 = k_1 + \delta, k_3 = \delta, k_4 = -k_1$, $a = b = 1$ and $\delta = 10^{-5}$, which are identical to the settings of TC5 as in the table within Fig 14. Dashed lines mark far-field soliton centre-lines used to make the domain $\sim X$-periodic.

References

Ablowitz, M. J. and Baldwin, D. E.: Nonlinear shallow ocean-wave soliton interactions on flat beaches, Phys. Rev. E, 86, 036 305, https://doi.org/10.1103/PhysRevE.86.036305, 2012.

Ablowitz, M. J. and Curtis, C. W.: Conservation Laws and Web-Solutions for the Benney–Luke Equation, Proc. Roy. Soc. A, 469, 16 pp., 2013.

Alnaes, M.: UFL: a finite element form language, In: Automated Solution of Differential Equations by the Finite Element Method by Logg, and Mardal and Wells (Eds), 2011.

Alnaes, M., Logg, A., Oelgaard, K., Rognes, M., and G.N., W.: Unified Form Language: A domain-specific language for weak formulations of partial differential equations, Tech. rep., https://arxiv.org/pdf/1211.4047.pdf, 2013.

Bai, W. and Eatock Taylor, R.: Higher-order boundary element simulation of fully nonlinear wave radiation by oscillating vertical cylinders, Applied Ocean Research, 28, 247–265, https://doi.org/https://doi.org/10.1016/j.apor.2006.12.001, 2006.

Bercea, G.-T., McRae, A. T. T., Ham, D. A., Mitchell, L., Rathgeber, F., Nardi, L., Luporini, F., and Kelly, P. H. J.: A structure-exploiting numbering algorithm for finite elements on extruded meshes, and its performance evaluation in Firedrake, Geoscientific Model Development, 9, 3803–3815, https://doi.org/10.5194/gmd-9-3803-2016, 2016.

Bingham, H. B. and Zhang, H.: On the accuracy of finite-difference solutions for nonlinear water waves, Journal of Engineering Mathematics, 58, 211–228, https://doi.org/https://doi.org/10.1007/s10665-006-9108-4, 2007.

Bokhove, O.: Variational water-wave modeling: from deep water to beaches, in: The Mathematics of Marine Modelling, pp. 103–134, Springer, https://link.springer.com/book/10.1007/978-3-031-09559-7, 2022.

Bokhove, O.: TCs3Dnumericalwavetank2022ff, https://doi.org/10.5281/zenodo.16919659, 2025.

Bokhove, O. and Kalogirou, A.: Variational water wave modelling: from continuum to experiment, in: Lectures on the theory of water waves, edited by Bridges, T., Groves, M., and Nicholls, D., vol. 426 of *LMS Lecture Note Series*, pp. 226–260, Cambridge University Press, 2016.

Bolton, J., Bokhove, O., Borman, D., Kalogirou, A., and Thompson, H.: Towards optimization of a wave-to-wire energy device in a breakwater contraction, in: European Wave Tidal Energy Conf. proceedings, Plymouth Sept. 2021, p. 10, 2021.

Bunnik, T.: Benchmark workshop on numerical wave modelling—description of test cases, Tech. Rep. 70022-1-RD, MARIN, 2010.

Burns, K., Vasil, G., Oishi, J., Lecoanet, D., and Brown, B.: Dedalus: a flexible framework for numerical simulations with spectral methods, Physical Review Research, 2, https://dedalus-project.org/, 2020.

Cai, X., Langtangen, H. P., Nielsen, B. F., and Tveito, A.: A Finite Element Method for Fully Nonlinear Water Waves, J. Comp. Phys., 143, 544–568, https://doi.org/https://doi.org/10.1006/jcph.1998.9997, 1998.

Choi, J., Bokhove, O., Kalogirou, A., and Kelmanson, M. A.: Numerical experiments on extreme waves through oblique-soliton interactions, Water Waves, 4, 139–179, 2022.

Choi, J., Kalogirou, A., Lu, Y., Bokhove, O., and Kelmanson, M.: A study of extreme water waves using a hierarchy of models based on potential-flow theory, Water Waves, 4, 139–179, 2024.

Engsig-Karup, A., Bingham, H., and Lindberg, O.: An efficient flexible-order model for 3D nonlinear water waves, J. Comp. Phys., 228, 2100–2118, https://doi.org/https://doi.org/10.1016/j.jcp.2008.11.028, 2009.

Engsig-Karup, A., Eskilsson, C., and Bigoni, D.: A stabilised nodal spectral element method for fully nonlinear water waves, Journal of Computational Physics, 318, 1–21, https://doi.org/https://doi.org/10.1016/j.jcp.2016.04.060, 2016.

Engsig-Karup, A. P. and Eskilsson, C.: Spectral Element FNPF Simulation of Focused Wave Groups Impacting a Fixed FPSO-type Body, Int. J. Offshore and Polar Engineering, 29, 141–148, https://doi.org/10.17736/ijope.2019.jc753, 2019.

Fochesato, C. and Dias, F.: A fast method for nonlinear three-dimensional free-surface waves, Proc. Royal Society A: Mathematical, Physical and Engineering Sciences, 462, 2715–2735, https://doi.org/10.1098/rspa.2006.1706, 2006.

Fochesato, C., Grilli, S., and Dias, F.: Numerical modeling of extreme rogue waves generated by directional energy focusing, Wave Motion, 44, 395–416, https://doi.org/https://doi.org/10.1016/j.wavemoti.2007.01.003, 2007.

Gagarina, E., Ambati, A., van der Vegt, J., and Bokhove, O.: Variational space-time (dis)continuous Galerkin method for nonlinear free surface water waves, J. Comp. Phys., 275, 459–483, 2014.

Gidel, F.: Variational water-wave models and pyramidal freak waves, Ph.D. thesis, University of Leeds, http://etheses.whiterose.ac.uk/21730/, 2018.

Gidel, F., Bokhove, O., and Kalogirou, A.: Variational modelling of extreme waves through oblique interaction of solitary waves: application to Mach reflection, Nonlinear Proc. Geophys., 24, 43–60, 2017.

Gidel, F., Lu, Y., Bokhove, O., and Kelmanson, M.: Variational and numerical modelling strategies for cost-effective simulations of driven free-surface waves, preprint at https://eartharxiv.org/repository/view/3411/, 2022.

Grilli, S., Horrillo, J., and Guignard, S.: Fully Nonlinear Potential Flow Simulations of Wave Shoaling Over Slopes: Spilling Breaker Model and Integral Wave Properties, Water Waves, 2, 263–297, https://doi.org/https://doi.org/10.1007/s42286-019-00017-6, 2020.

Grilli, S. T., Guyenne, P., and Dias, F.: A fully non-linear model for three-dimensional overturning waves over an arbitrary bottom, Int. J. Numerical Methods in Fluids, 35, 829–867, https://doi.org/https://doi.org/10.1002/1097-0363(20010415)35:7<829::AID-FLD115>3.0.CO;2-2, 2001.

Hairer, E., Lubich, C., and Wanner, G.: Geometric numerical integration illustrated by the Störmer-Verlet method, Acta Numerica, 12, 399–450, 2003.

Ham, D. A., Kelly, P. H. J., Mitchell, L., Cotter, C. J., Kirby, R. C., Sagiyama, K., Bouziani, N., Vorderwuelbecke, S., Gregory, T. J., Betteridge, J., Shapero, D. R., Nixon-Hill, R. W., Ward, C. J., Farrell, P. E., Brubeck, P. D., Marsden, I., Gibson, T. H., Homolya, M., Sun, T., McRae, A. T. T., Luporini, F., Gregory, A., Lange, M., Funke, S. W., Rathgeber, F., Bercea, G.-T., and Markall, G. R.: Firedrake User Manual, Imperial College London and University of Oxford and Baylor University and University of Washington, first edition edn., https://doi.org/10.25561/104839, 2023.

Homolya, M. and Ham, D. A.: A Parallel Edge Orientation Algorithm for Quadrilateral Meshes, SIAM J. Scientific Computing, 38, S48–S61, https://doi.org/10.1137/15M1021325, 2016.

Kadomtsev, B. and Petviashvili, V.: On the stability of solitary waves in weakly dispersive media, Sov. Phys. Dokl., 15, 539–541, 1970.

Karniadakis, G. and Sherwin, S.: Spectral/hp Element Methods for Computational Fluid Dynamics, Oxford University Press, https://doi.org/10.1093/acprof:oso/9780198528692.001.0001, 2005.

Kodama, Y.: KP solitons in shallow water, J. Phys. A: Mathematical and Theoretical, 43, 434–484, 2010.

Kodama, Y.: Solitons in two-dimensional shallow water, SIAM, Philadelphia, (Exercise 6.7), 2018.

Li, B. and Fleming, C. A.: A three dimensional multigrid model for fully nonlinear water waves, Coastal Engineering, 30, 235–258, https://doi.org/https://doi.org/10.1016/S0378-3839(96)00046-4, 1997.

Lin, Z., Qian, L., Bai, W., Ma, Z., Chen, H., Zhou, J.-G., and Gu, H.: A Finite Volume Based Fully Nonlinear Potential Flow Model for Water Wave Problems, Applied Ocean Research, 106, 102 445, https://doi.org/https://doi.org/10.1016/j.apor.2020.102445, 2021.

Lu, Y.: Numerical Wavetanks for Wave Generation, Interaction, and Dissipation: Variational and Computational Modelling, Ph.D. thesis, University of Leeds, 2025.

Luke, J.: A variational principle for a fluid with a free surface, J. Fluid Mech., 27, 395–397, 1967.

Ma, Q. and Yan, S.: Quasi ALE finite element method for nonlinear water waves, J. Comp. Phys., 212, 52–72, https://doi.org/https://doi.org/10.1016/j.jcp.2005.06.014, 2006.

Ma, Q. W. and Yan, S.: QALE-FEM for numerical modelling of non-linear interaction between 3D moored floating bodies and steep waves, Int. J. Nume. Meth. Eng., 78, 713–756, https://doi.org/https://doi.org/10.1002/nme.2505, 2009.

Ma, Q. W., Wu, G. X., and Eatock Taylor, R.: Finite element simulation of fully non-linear interaction between vertical cylinders and steep waves. Part 1: methodology and numerical procedure, Int. J. Num. Methods in Fluids, 36, 265–285, https://doi.org/https://doi.org/10.1002/fld.131, 2001.

McRae, A. T. T., Bercea, G.-T., Mitchell, L., Ham, D. A., and Cotter, C. J.: Automated Generation and Symbolic Manipulation of Tensor Product Finite Elements, SIAM J. Scientific Computing, 38, S25–S47, https://doi.org/10.1137/15M1021167, 2016.

Miles, J. W.: Obliquely interacting solitary waves, J. Fluid Mech., 79, 157–169, 1977.

Ning, D.-Z., Shi, J., Zou, Q.-P., and Teng, B.: Investigation of hydrodynamic performance of an OWC (oscillating water column) wave energy device using a fully nonlinear HOBEM (higher-order boundary element method), Energy, 83, 177–188, https://doi.org/https://doi.org/10.1016/j.energy.2015.02.012, 2015.

Ritchie, S.: Science fictions: Exposing fraud, bias, negligence and hype in science, Vintage UK, Dublin, 2021.

Salwa, T., Bokhove, O., and Kelmanson, M.: Variational modelling of wave-structure interactions with an offshore wind-turbine mast, J. Eng. Math., 107, 61–85, https://doi.org/https://doi.org/10.1007/s10665-017-9936-4, 2017a.

Salwa, T., Bokhove, O., and Kelmanson, M.: Variational modelling of wave-structure interactions with an offshore wind-turbine mast, J. Eng. Math., 107, 61–85, 2017b.

Smith, G. D.: Numerical Solution of Partial Differential Equations: Finite-difference methods, p. 217, Clarendon Press, Oxford, 2nd. edn., 1978.

Wang, W., Kamath, A., Pakozdi, C., and Bihs, H.: Investigation of Focusing Wave Properties in a Numerical Wave Tank with a Fully Nonlinear Potential Flow Model, J. Marine Science and Eng, 7, https://doi.org/10.3390/jmse7100375, 2019.

Windt, C., Davidson, J., and Ringwood, J. V.: High-fidelity numerical modelling of ocean wave energy systems: A review of computational fluid dynamics-based numerical wave tanks, Renewable and Sustainable Energy Reviews, 93, 610–630, https://doi.org/https://doi.org/10.1016/j.rser.2018.05.020, 2018.

Wu, G. and Eatock Taylor, R.: Finite element analysis of two-dimensional non-linear transient water waves, Applied Ocean Research, 16, 363–372, https://doi.org/https://doi.org/10.1016/0141-1187(94)00029-8, 1994.

Wu, G. and Eatock Taylor, R.: Time stepping solutions of the two-dimensional nonlinear wave radiation problem, Ocean Engineering, 22, 785–798, https://doi.org/https://doi.org/10.1016/0029-8018(95)00014-C, 1995.

Wu, G., Ma, Q., and Eatock Taylor, R.: Numerical simulation of sloshing waves in a 3D tank based on a finite element method, Applied Ocean Research, 20, 337–355, https://doi.org/https://doi.org/10.1016/S0141-1187(98)00030-3, 1998.

Xu, H., Cantwell, C. D., Monteserin, C., Eskilsson, C., Engsig-Karup, A. P., and Sherwin, S. J.: Spectral/hp element methods: Recent developments, applications, and perspectives, J. Hydrodynamics, 30, 1–22, https://doi.org/10.1007/s42241-018-0001-1, 2018.

Yan, S. and Ma, Q.: Numerical simulation of fully nonlinear interaction between steep waves and 2D floating bodies using the QALE-FEM method, J. Comp. Phys., 221, 666–692, https://doi.org/https://doi.org/10.1016/j.jcp.2006.06.046, 2007.

Yan, S. and Ma, Q. W.: QALE-FEM for modelling 3D overturning waves, Int. J. Numer. Meth. in Fluids, 63, 743–768, https://doi.org/https://doi.org/10.1002/fld.2100, 2010.